Permanent Magnet Motor Simulation

For the Nuon Solar Team

D. J. Buist and E. H. Salzmann

Technische Universiteit Delft

TU Delft Delft University of Technology

Challenge the future

PERMANENT MAGNET MOTOR SIMULATION

FOR THE NUON SOLAR TEAM

by

D. J. Buist and E. H. Salzmann

in partial fulfillment of the requirements for the degree of

Bachelor of Science
in Electrical Engineering

at the Delft University of Technology,
to be defended publicly on Tuesday January 30, 2018 at 12:30 PM.

Supervisor:	dr. ir. P. J. van Duijsen	TU Delft
Thesis committee:	prof. dr. ir. W. A. Serdijn (Chair)	TU Delft
	dr. ing I. E. Lager	TU Delft
	C. van Wezel BSc.	Nuon Solar Team

This thesis is confidential and cannot be made public until January 30, 2023.

TU Delft Delft University of Technology

PREFACE

0.1. ABSTRACT

This thesis is about the simulation of the permanent magnet motors of the Nuna Solar Car in order to find their fundamental motor parameters. These parameters can then be used in a Field-Oriented control algorithm to be used in a new motorcontroller for the team. A finite element analysis is done on the two current motors of the Nuna solar car, a radial flux Mitsuba motor and an axial flux Marand motor, with the intend to find the fundamental motor parameters, the phase resistance, the inductance and the motor constant.

The model is presented and the simulation results are discussed. Also some variations to the current design have been made to test the adaptability of the simulation. Also some work is done to simulate the entire drive system of the car.

0.2. ACKNOWLEDGEMENTS

First and foremost, the team would like to thank dr.ir. Peter van Duijsen for his enthusiastic supervision of the work, the mini lectures and inspiration for research possibilities. Despite the relatively late start to the project, the team was able to kick-start the work due to his extensive knowledge of the field and experience with comparable projects.

Furthermore we would like to thank the Nuon Solar Team for assigning the project to us and being very supportive when the group needed some more information about certain dimensions or properties of the car and motor. Special thanks go out to Bas van Wee and Casper van Wezel for acting as daily supervisors from the Nuon Solar Team.

Also we would like to mention dr.ing. Ioan Lager for coordinating the Bachelor Graduation Project just for the four of us, prof.dr.ir. Wouter Serdijn for serving on our thesis committee, dr.ir. Jianning Dong for his enthusiastic help with some questions and ir. Bart Roodenburg for creating some private workspace within EEMCS.

Finally we like to thank our co-group members, Jelle Bout and Tobias Roest, for the enjoyable 10 weeks working together and especially our families for bearing with us through our years of studying. Without their support this thesis would not have seen the light of day.

D. J. Buist and E. H. Salzmann
Delft, January 2018

CONTENTS

LIST OF SYMBOLS & ABBREVIATIONS

AC	Alternating Current
BLDC	Brushless Direct Current
CAN	Controller Area Network
CSI	Current Source Inverter
DC	Direct Current
EMF	Electromotive Force
EV	Electric Vehicle
FOC	Field Oriented Control
IGBT	Insulated-Gate Bipolar Transistor
IPM	Interior Permanent Magnet
MC	Motor Controller
MCU	Microcontroller unit
MOSFET	Metal-Oxide-Semiconductor Field-Effect Transistor
OCTW	Overcurrent & overtemperature warning
PM	Permanent Magnet
PMSM	Permanent Magnet Synchronous Motor
PWM	Pulse Width Modulation
SPM	Surface-Mounted Magnet
SVM	Space vector modulation
VFD	Variable Frequency Drive
VSI	Voltage Source Inverter

1

INTRODUCTION

This thesis is carried out with the Nuon Solar Team as partial fulfillment for the bachelor Electrical Engineering at the Delft University of Technology. The Bachelor graduation project is a complex educational activity offering the students the possibility to materialize the knowledge and practical skills accumulated during the complete Bachelor curriculum in a design project in the area of Electrical Engineering. The students are expected to go through the complete design process, from drawing up a set of requirements, through the concept analysis and design, concept selection, to the presentation of the final design, in a structured and iterative manner. The full project for the Nuna is done by one group of 4 students, split up in 2 subgroups each working on different aspects.

1.1. PROBLEM DEFINITION

The Nuon Solar Team is a team consisting out of 16 students, designing, building and eventually racing a car only on solar energy. The team participated eight times in the bi-annual race World Solar Challenge in Australia, the world championship for solar car racing. The team became a world champion seven times and a runner-up twice. Besides the race in Australia the team won the Sasol Solar Challenge in South Africa in 2014 and 2016.

Crucial in successfully completing this 3000km journey through the dessert of Australia is an efficient and reliable motor controller (MC). This MC is connected to the single motor of Nuna and must stay up and running all the time. The MC delivers power to the motor while driving and delivers energy back to the battery pack when breaking. Apart from delivering power, information needs to be measured from the motor and the controller. Different temperatures, currents, voltages and speed needs to be measured and sent through a CAN-bus. As all electrical components in the car communicate with each other via a digital protocol (CAN), it is important that this future MC is capable of transmitting and receiving data via this protocol.

Critical in the correct control is thorough knowledge about the motors used. The Nuna Solar Car is of course powered by an electric motor. Both the drive and motor are of the shelf products. The current Nuna motor is the Mitsuba M2096D, a brushless direct current (BLDC) motor. This motor has concentrated windings and radially magnetized magnets in the rotor. The previous motor is the Marand Axial Flux Wheel Motor. Due to a lower performance at a lower battery voltage this motor has been replaced by the Mitsuba motor.
The motor is controlled by the Tritium WaveSculptor 22. At low speed the controller provides current in a trapezoidal form and at higher speeds, the current is sinusoidal. Also the drive system suffered from too low power ratings (which made it hard to go uphill) and significant torque ripples.
The Mitsuba motor comes with its own motorcontroller. This controller provides a power high enough for the car, but is less efficient.
Currently the knowledge about the complete motor drive system is limited. Especially the Tritium control unit is a black box to the team. This is why one of their research goals this year is finding out the opportunities regarding developing their own motor drive system.

1.2. RESEARCH GOALS

As a full team it was decided that the focus of the project would be on developing a new motor controller since the current setup has many unknowns in terms of components and working principles. This was preferred over an off-the-shelf product as the team then would have full control and flexibility in the design and thorough knowledge of all the systems in the car.

A design needs to be made for a modern, sensorless controller, capable of handling the power requirements. This was decided because sensorless control should be more efficient and flexible and, most importantly, would increase reliability and hardware simplicity as it reduces wiring and the need for expensive hardware like encoders or resolvers.

However, such a project would be far too large to complete within the set time frame of 10 weeks. Therefore our study would focus on subparts of the design, so that other people can follow up on it and complete the design.

Knowing the fundamental motor parameters is essential in sensorless control. So here the work was split up in two. One group would focus on motor simulations to find these fundamental parameters and possibly some improvements, while the other group would use these parameters in their implementation of the Field Oriented Control (FOC) algorithm.

The FOC algorithm needs to control the motor by using an inverter. The design of this inverter depends highly on the characteristics of the motor and control software. A brief outline will be given about the topology and working principle of an inverter as well as a quick preview for a future design of the inverter to be designed later.

Because motor and controller have a huge dependency when it comes to efficiency, this subgroup would also develop a simulation in which FOC is assumed as working, to check their efficiency in the whole system. To achieve these goals, therefore two deliverables will be made. Considerations will be discussed in the following chapters.

1. A model of the Mitsuba and Marand motors to calculate the motor parameters and losses of different configurations, like different windings, different magnets etc. These results will be verified against datasheet values and measurements of actual motors.
2. A flexible simulation with FOC, different kind of inverters and different kind of motor configurations to simulate the efficiency of the motor in combination with the control.

1.3. DOCUMENT STRUCTURE

This thesis is structured in the following way. First it will give some background knowledge about the essentials for understanding this thesis. The working principle and common structures of AC motors will be introduced. Also more in depth topics like winding patterns and magnet design considerations will be mentioned.

After that it will dive into the work done by the the group. First it will discuss methods, reasons and results of the motor model. Next, these results will be used in the developed drive model which is discussed in the following chapter.

After the work done, some conclusions are drawn and recommendations are made for further research to be done for completing an entire motor drive.

2

BACKGROUND

This chapter is intended to get readers not familiar with electric motors and control up to speed with the existing techniques, technologies and nomenclature. As the world of electric motors is incredibly vast, only those things that have a direct connection to the remainder of the thesis will be discussed and this chapter is therefore not meant as a comprehensive guide to electric motor control for all applications.

2.1. AC MOTORS

There is a lot of ambiguity towards the difference between AC and DC motors. The most commonly used distinction seems to be their drive signal, which can be either alternating current or direct current. Therefore we refer to AC motors as those which are designed to work with an AC power source to convert electrical energy in mechanical power.

An overview of common forms of AC motors can be seen in figure 2.1. For this thesis we will focus on Permanent Magnet Synchronous Motors (PMSM), which will be discussed further in the following sections.

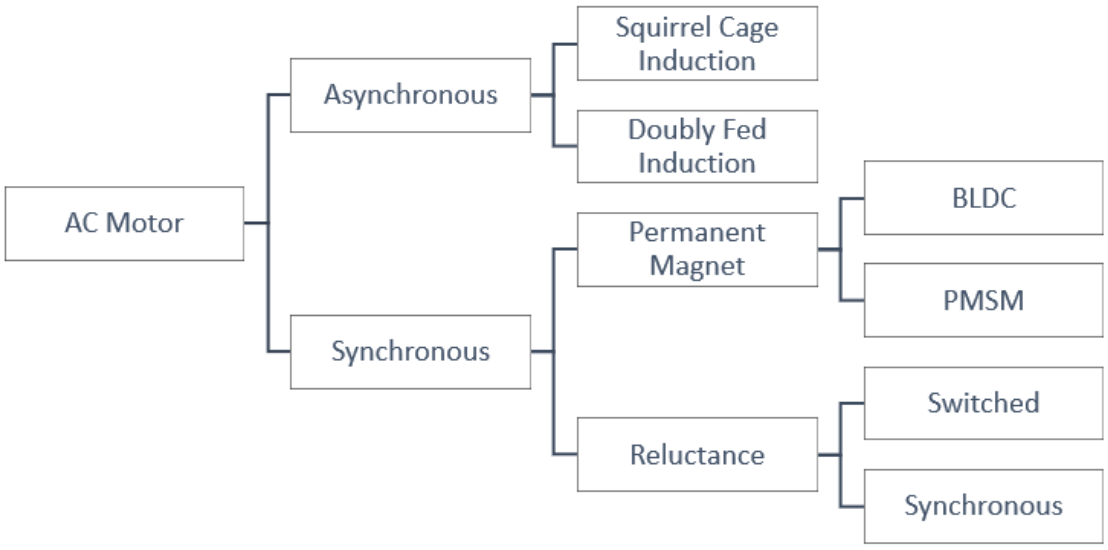

Figure 2.1: Taxonomy of AC Motors [1]

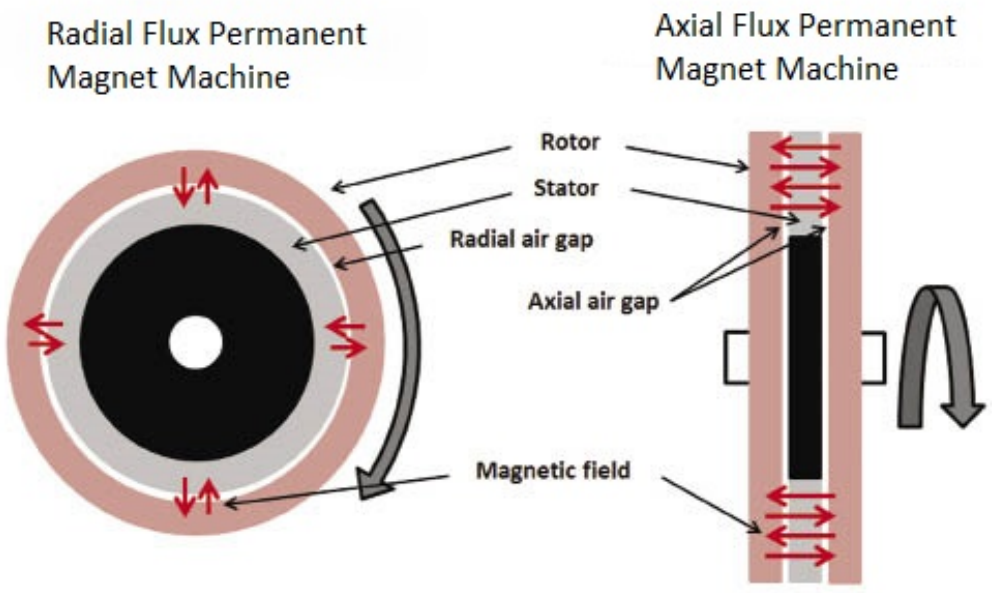

Figure 2.2: Intersection of a radial flux machine and an axial flux machine.

2.1.1. PERMANENT MAGNET MOTOR

Electric motors operate through an interaction between its magnetic field and winding currents to generate force. They consist of two main components, the stator and the rotor. The rotor is the moving part of the motor, which turns the shaft or wheel to produce mechanical power. The stator is the stationary part of the motor and usually consists of windings or permanent magnets. The stator core is made up of many thin metal sheets, called laminations. Laminations are used to reduce energy losses that would result if a solid core were used.

A permanent magnet (PM) motor is a type of brushless electric motor where the principal field is produced by permanent magnets rather than field windings. The stator carries the windings and the magnets are placed on the rotor. The space between the stator and rotor is called the air gap. See Figure 2.2.

By running a current through the 3-phase windings, the windings create a magnetic field with a north and south pole. Through the attraction of the permanent magnets and the field produced the rotor will start rotating until it is aligned with the magnetic field. By constantly changing the current run through the windings a rotating magnetic field can be produced and continuous motion of the rotor is established.

The rotor of PM motors can be placed inside the stator or outside, respectively called inrunner or outrunner. The design of choice often depends on the load that needs to be driven. If the motor is connected to the load by a shaft, then an inrunner is an obvious choice, but for direct-drive purposes the outrunner type is commonly used. With an inrunner configuration, the motor can have a smaller overall motor diameter, lower rotor inertia and possibly better winding heat dissipation. Outrunners typically have a higher inertia which may be desirable in constant-speed applications[2].

Another important distinction to be made is the difference between radial and axial flux machines. Radial machines produce a radial magnetic flux, while axial machines give a flux in the axial direction across the air gap. Radial machines are far more popular, given their simplicity in manufacturing and assembly as axial machines need to be laminated in radial direction which is harder to produce. Axial machines, especially in a double rotor (or stator) configuration do have the possibility of higher power densities and are therefore gaining ground[3]. Axial machines are on average smaller in diameter. This means reduced weight and core losses. This weight reduction is however cancelled by the increase in magnet weight if a double rotor configuration is used.

There is also room for experimentation with the placement of the permanent magnets. The magnets can be placed inside the rotor, called Interior Permanent Magnet (IPM) or on the surface, called Surface-Mounted Magnet (SPM). The surface-mounted magnets are most commonly used since their construction is much easier compared to IPM where the magnets need to be embedded in the rotor yoke. Figure 2.3 shows the different configurations possible. Figure (a) and (b) display SPM, where in (b) there are special cavities in

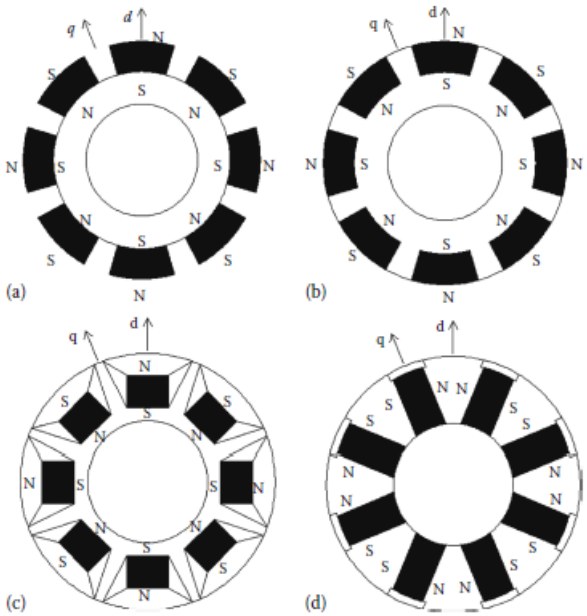

Figure 2.3: (a) Surface PM (SPM) synchronous machine. (b) Surface inset PM (SIPM) synchronous machine. (c) Interior PM (IPM) synchronous machine. (d) Interior PM synchronous machine with circumferential orientation[3]

the rotor yoke for the magnets. Figures (c) and (d) are IPM rotors.

A key characteristic of electric motors is the induced back electromotive force (back EMF), which is produced as counter reaction to the rotating magnetic field. Rotor flux linkage, λ, is a function of rotor angular position. Back EMF, E, is the rate of change of rotor flux linkage in the winding. Therefore, the amplitude of the back EMF waveform is a function of angular velocity and the shape is a function of angular position. Some factors influencing the shape are: magnet geometry, magnetization, stator core geometry, and winding distribution. These are all properties of the motor itself, and do not depend on the drive. Two dominant shapes of back EMF often evaluated are trapezoidal and sinusoidal, where BLDC motors typically have a more trapezoidal back EMF and PMSMs a more sinusoidal one.

2.1.2. MAGNET STRUCTURES

For a radial flux PM machine the magnets are normally curved. The magnetization of these magnets can either be parallel or radial. In Figure 2.4 the difference is illustrated. From past research it can be concluded that radial magnetization presents slightly lower losses compared with parallel magnetized magnets, but these losses are almost neglectable for machines with small magnets and small power. Furthermore, the production of radial magnetized magnets require a lot of advanced tools and knowledge[4].

Another way to configure the magnets in the rotor is by using Halbach arrays. The advantages of this technique are an almost perfect sinusoidal back EMF and low cogging torque among others[5]. An ideal Halbach magnet has an perfect sinusoidal magnetization, however this is impossible to produce. So this magnet is built of different magnetized parts in one array. This array cancels either below or above the magnet array as shown in Figure 2.5.

The magnetic field of different magnetized magnets is illustrated in Figure 2.6. In the parallel magnetized rotor, the field lines are parallel. The field lines for radial magnetized magnets are radial. But apart from the magnets the field strength of the other parts are not much influenced by the type of the magnets. However, for halbach array 1 the field lines cancel out below, which is clearly visible, so the field lines are more concentrated in one tooth. For halbach array 2 the field lines cancel out above, where the field lines are distributed among multiple teeth compared to halbach array 1. Which magnet configuration works best depend on the application and the money available.

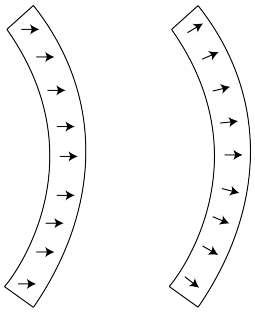

Figure 2.4: Magnetization of magnets in rotor, parallel (left) and radial (right)

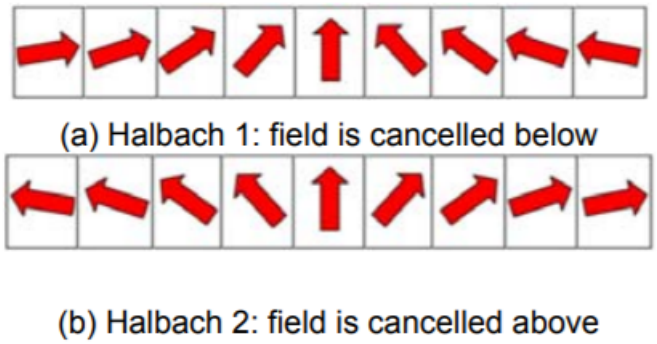

Figure 2.5: Two ways to establish Halbach arrays[5]

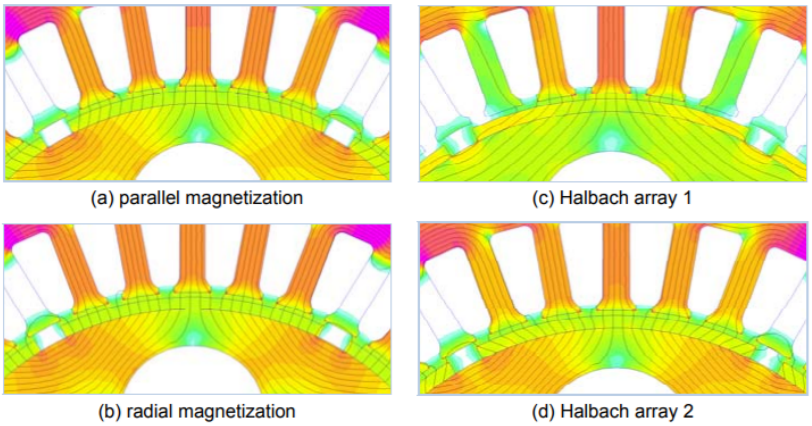

Figure 2.6: Magnetic field of various types of magnetization of an inrunner motor[5]

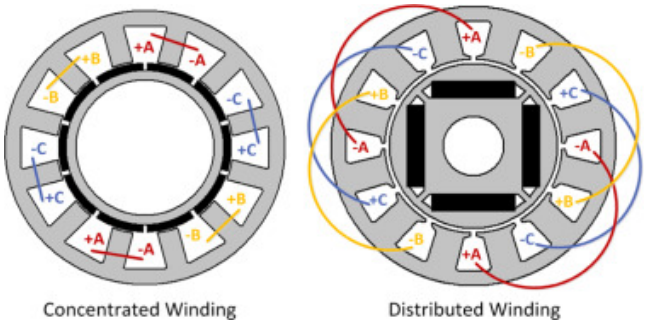

Figure 2.7: Concentrated versus distributed winding[6]

2.1.3. WINDING PATTERNS

The pattern of the coil windings is important for the efficiency of the motor. A pattern can be classified on the basis of different specifications.

Concentrated versus distributed winding The distribution of the windings can either be concentrated or distributed. Concentrated windings means that a phase is wound around one tooth, which means that the phases are non-overlapping. Traditionally, this term is used for windings having one slot per pole per phase, but currently, this term is normally used to indicate that windings are non-overlapping. When the number of slots per pole per phase is an integer the winding is called integer-slot.
Distributed windings on the other hand have multiple slots per pole per phase. In Figure 2.7 the difference between concentrated and distributed windings is shown. The disadvantage of distributed windings is the higher copper losses as result of the overlapping end-windings. Concentrated windings deliver good field-weakening performance, but also produce more space harmonics [6].

Single-layered versus double-layered windings Every slot can have either one or two layers. When the stator is single-layered, like in Figure 2.8a, the windings are wound on alternating teeth. Double-layered windings divide the slot into two parts vertically and each tooth has its own coil, like in Figure 2.8b. Double-layer windings have better properties such as shorter end-windings and more sinusoidal back-emf waveforms than one-layer windings.

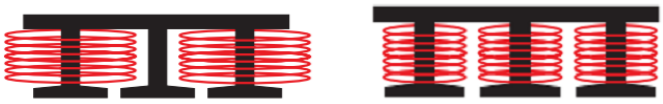

(a) Single-layer winding (b) Double-layer winding

Figure 2.8: Two types of layered windings[7]

Full pitch versus short pitch windings The slot pitch is a measurement for the width of the coil windings. This degree is a ration between the magnets and the windings. If the coil sides of one winding lies under opposite poles, the coil winding is called full pitch. If the coil is wound less than 180° electrical, like the slot pitch in Figure 2.9a, the coil is called a short pitch coil. If the coil is wound 180° electrical, like in Figure 2.9b, the coil is called full pitch coil. Full pitching induces the maximum back EMF. Short pitching eliminates high frequency harmonics which distort the sinusoidal nature of EMF, so the back-EMF is more sinusoidal due to short pitching. And as high frequency harmonics get eliminated, eddy current and hysteresis losses which depend on frequency also get minimized. This increases the efficiency.

One way to classify the windings is with the winding factor. This factor expresses the difference between the flux of the specified winding pattern and flux that would have been linked by a single-layer full-pitch non-skewed (field of the magnets is perpendicular or parallel with the field of the windings) integer-slot winding with the same number of turns and one single slot per pole per phase. An example of a winding configuration

with winding factor 1.0 is a single-layer 2-pole 6-slot integer-slot winding. This factor can be calculated with equation 2.1. This fundamental winding factor is proportional with the torque.

$$k_w = k_p \cdot k_d \cdot k_s, \tag{2.1}$$

where $k_p = cos(a/2)$ is the pitch factor that represents the pitch, a is the value of by which the coil is short-pitched. For a full-pitch wound motor $k_p = 1$.
And k_d is the distribution factor which reflects the number of poles one phase is distributed on. When one phase is wound around multiple neighboring teeth this constant will be lower compared to a motor where the phase is wound around one slot.
Last, k_s is the skew factor. This is 1 for most motors, but can be less than one when the rotor bars are twisted, for example in a squirrel-cage motor[8].

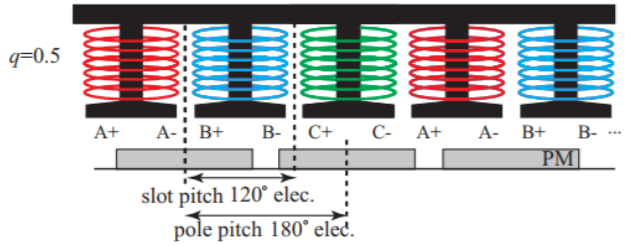

(a) One pole per slot per phase

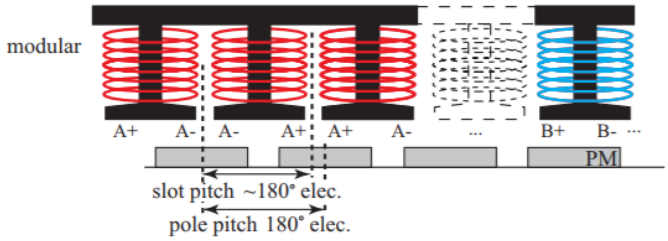

(b) Multiple poles per slot per phase

Figure 2.9: Two types of concentrated windings[7]

Another parameter to describe the rotor and corresponding winding patterns is q, the number of slots Q_s per pole p per phase, so:

$$q = \frac{Q_s}{3p} \tag{2.2}$$

The higher q, the more sinusoidal the back EMF and thus the lower the torque ripple and losses.

2.1.4. COMPARISON

A motor can be characterized by its torque-speed curve. An ideal curve can be found in Figure 2.10. The dependencies of the motor are

$$\tau = K \cdot i \tag{2.3}$$

$$E = K \cdot \omega, \tag{2.4}$$

where τ is torque, K is a motor constant, i is the phase current, E is the back EMF and ω is the angular speed. A motor can have a constant torque until the back EMF reaches the battery voltage, because combining Equations 2.3 and 2.4 gives $\tau = E \cdot i/\omega$. At the point where the battery voltage is reached, the torque will decrease with $E \cdot i/\omega = P/\omega$, this is called the constant power region. The point where the constant torque region stops and the constant power region begins, the speed is the base speed. This base speed should be around the cruise speed of a car.

A BLDC motor is mostly used in high speed applications (over 5000 rpm), where it performs best as can be seen in figure 2.11. A BLDC motor is in general better than a PMSM in terms of nominal speed at low power. This also holds for acceleration at low power, as shown in Figure 2.12, however, for higher power levels, a

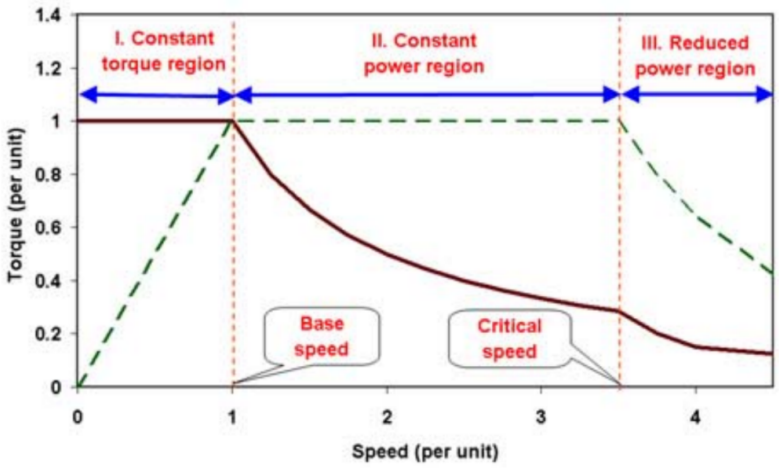

Figure 2.10: Idealized torque/power-speed characteristics. The solid line is the torque and the dashed line the power.[9]

BLDC motor stops accelerating, where a PMSM performs better. In Figure 2.13 three different kinds of motor are compared for different criteria. These motors are the same as the motors in Figures 2.11 and 2.12.

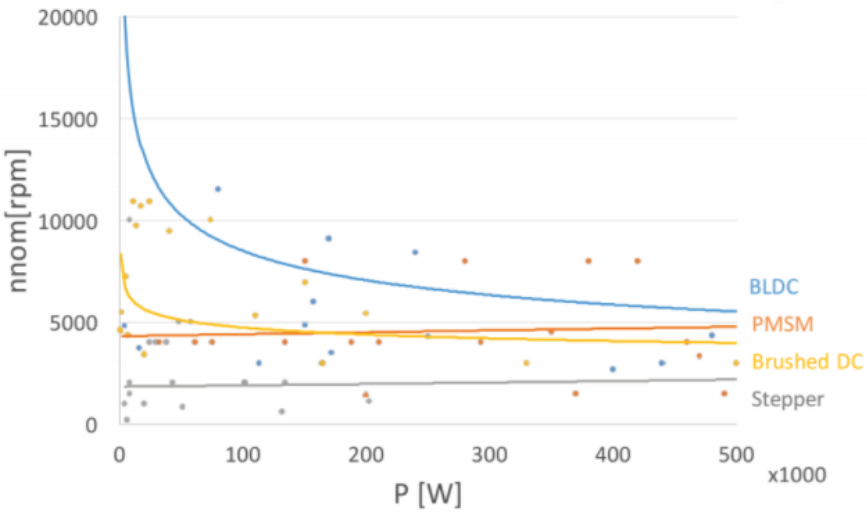

Figure 2.11: Nominal motor speed compared to rated power [10]

With a DC-drive a BLDC motor has torque ripple at commutations. The PMSM has no torque ripple at commutation.

In Magnussen et al. [11] three different surface-mounted permanent magnet synchronous motors are compared, machine A has distributed windings, machine B has concentrated windings with winding factor 0.87 and machine C has concentrated windings with winding factor 0.95. In Table 2.1 the machines are compared at different criteria. It is shown that the two motors with concentrated windings have higher inductance, due to higher slot leakage. The motors with concentrated windings have a wider constant power region, as shown in Figure 2.14. The machine with distributed windings has a better performance in combination with the inverter compared to the motors with concentrated windings, as shown in Figure 2.15.

These papers show that it is hard to say which motor performs better for a solar car. On the one hand, a BLDC motor performs better in terms of nominal speed and maximum acceleration. On the other hand, a PMSM delivers a more constant torque and has a higher power density.
From the study with different winding patterns, it is clear that the motor with concentrated windings and a winding factor of 0.95 has the best performance. However, these motors do not only vary in winding patterns, but also in number of slots and dimensions. So even if it seems obvious that motors with concentrated

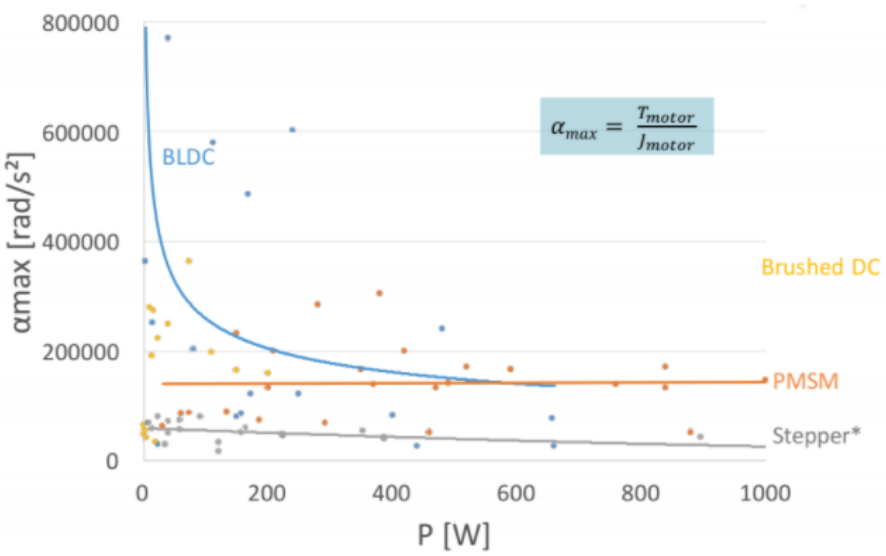

Figure 2.12: Maximum acceleration compared to motor power [10]

Figure 2.13: Comparison between different motor types [10]

Table II: Performance on different criteria (1: best, 4: worst)

Criterion	*Brushed DC*	*BLDC*	*PMSM*	*Stepping Motor*
Nominal speed	2-3	1	2-3	4
Nominal torque	4	3	2	1
Power Density	4	3	1	2
Maximum Acceleration	-	1	2	4
Overload capacity	1	2-3	2-3	4
Price	2	3	4	1

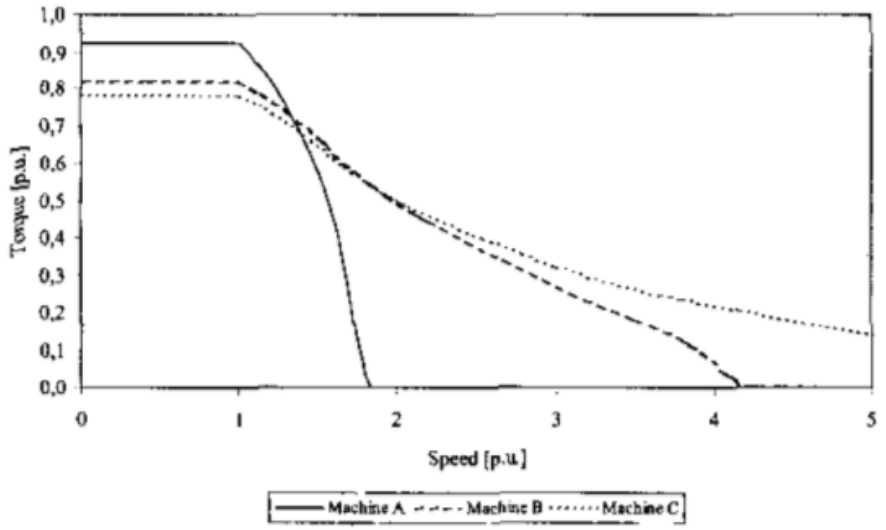

Figure 2.14: The normalized torque capability versus speed of the studied machine designs for an inverter rating of 20 kVA and a base speed of 2000 rpm.

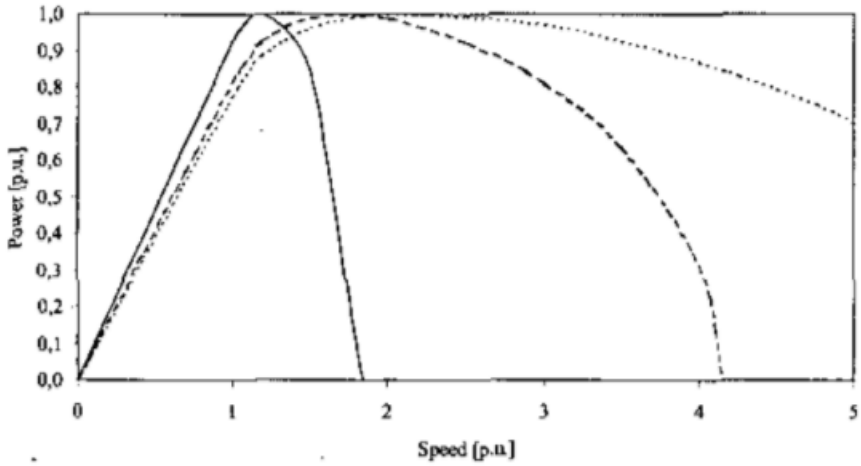

Figure 2.15: The normalized speed capability versus power of the studied machine designs for an inverter rating of 20 kVA.

Table 2.1: A relative comparison of three different surface-mounted permanent magnet synchronous machines. The used grades are: excellent: ++, good: +, fair: 0, poor: - and bad: –.

Machine	A	B	C
Power factor below base speed	++	+	0
Power factor above base speed	–	+	++
Power density	0	+	++
Cogging torque	–	0	++
Ripple torque	–	-	++
Efficiency	0	+	++

windings perform best, it is still important to verify this is also the case for the current Nuna motors.

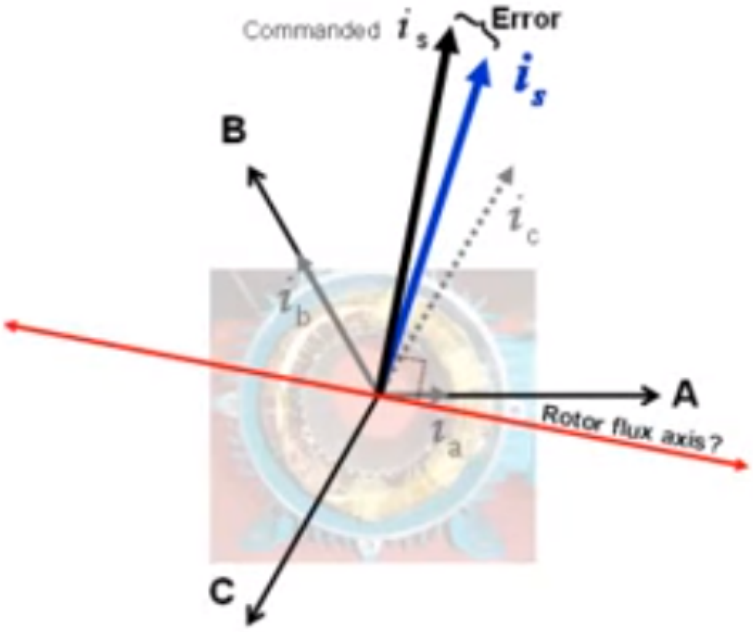

Figure 2.16: Commanded current space vector and actual current space vectors

2.2. FIELD ORIENTED CONTROL

High-performance motor control is characterized by smooth rotation over the entire speed range of the motor, full torque control at zero speed, and fast accelerations and deceleration. To achieve such control, one can use a technique called Field Oriented Control (FOC) for 3-phase AC motors. The basic idea of the FOC algorithm is to decompose the stator current into the magnetic field-generating part and the torque-generating part. Both components can be controlled separately after the decomposition. The structure of the motor controller is then as simple as that for separately excited DC motors.

Figure 2.17 shows the basic structure of the vector-control algorithm for the PMSM. The process follows the next steps:

1. Measure the motor quantities (phase voltages and currents).

   The stator current is measured to compare it to the rotor flux. Only two phases need to measured as the third can be deduced from Kirchoff's Current Law, this saves cost of an extra current sensor. The stator current produces a magnetic field vector,the magnetomotive force (MMF), which is the magnetic equivalent of the electromotive force (EMF). Therefore by controlling currents, one can produce a magnetic field of any direction and magnitude.

   Current space vectors are used for this purpose, as the current is much more easily measured than the magnetic field. A current space vector has the direction of the field produced by a winding and a magnitude proportional to the current. The sum of all windings produces a net current space vector. See Figure 2.16 for a graphic representation.

   Torque is produced through the interaction of this stator field and the rotor field. If the rotor and stator field are in the same direction, no net torque is produced. To get the maximum torque per amp, the MMF vector should be at a 90 degree angle compared to the rotor flux vector.

2. Transform them into the 2-phase system (α, β) using Clarke transformation.

   To simplify calculations the 3-phase reference frame system is converted to a 2-axis orthogonal stationary system using a mathematical operation known as the Clarke transform. This transform is expressed by the following equations

$$I_\alpha = \frac{2}{3}(I_a) - \frac{1}{3}(I_b - I_c) \tag{2.5}$$

$$I_\beta = \frac{2}{\sqrt{3}}(I_b - I_c), \tag{2.6}$$

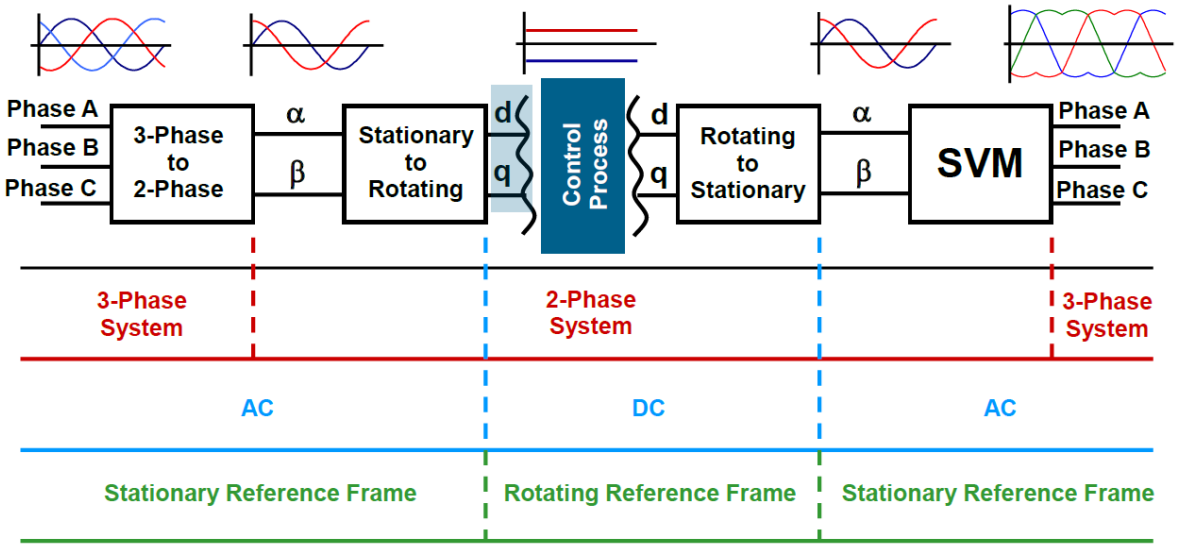

Figure 2.17: Field Oriented Control[12]

where I_a, I_b, I_c represent the 3-phase currents and I_α and I_β are the currents aligned to the α and β axes.

3. Transform the stator currents into the d, q reference frame using Park transformation.

   To further simplify calculations a technique is used to get the stationary current vectors in the same reference frame as the rotor, which has a rotational reference frame. For this the Park transform is used. The Park transform is computed through the following equations

$$I_d = I_\alpha * \cos\theta + I_\beta * \sin\theta \tag{2.7}$$

$$I_q = I_\beta * \cos\theta - I_\alpha * \sin\theta, \tag{2.8}$$

   where I_d and I_q are the current along the d- (direct) and q- (quadrature) axes. The direct axis is always aligned with the rotor angle and following from these derivations is that the quadrature axis is defined as to be orthogonal with the direct axis. In steady-state conditions, these are DC quantities, which makes them easier to regulate.

4. Generate correction signals.

   By using I_d and I_q and the reference values and error signal can be generated which corrects the position of the net current vector to that of the commanded vector. The I_d component can be used to control the rotor flux and the I_q component to control the torque output of the motor. These signals are input to two PI controllers, which amplify the correction signals and output two correction voltages V_d and V_q

5. The stator-voltage space vector is transformed by the inverse Park transformation back from the d, q reference frame into the 2-phase system fixed with the stator.

   The system has now produced two correction voltages in the rotating d-q reference frame. These however cannot be applied directly to a stationary 3-phase motor. Therefore the voltages need to be converted back to the $\alpha - \beta$ reference frame using the inverse Park Transform. The equations for this transform are as follows:

$$V_\alpha = V_d * \cos\theta - V_q * \sin\theta \tag{2.9}$$

$$V_\beta = V_q * \cos\theta + V_d * \sin\theta \tag{2.10}$$

Phase C	Phase B	Phase A	V_{ab}	V_{bc}	V_{ca}	V_{ds}	V_{qs}	Vector
0	0	0	0	0	0	0	0	$O(000)$
0	0	1	V_{DC}	0	$-V_{DC}$	$\frac{2}{3}V_{DC}$	0	U_0
0	1	1	0	V_{DC}	$-V_{DC}$	$\frac{V_{DC}}{3}$	$\frac{V_{DC}}{3}$	U_{60}
0	1	0	$-V_{DC}$	V_{DC}	0	$\frac{-V_{DC}}{3}$	$\frac{V_{DC}}{3}$	U_{120}
1	1	0	$-V_{DC}$	0	V_{DC}	$\frac{-2V_{DC}}{3}$	0	U_{180}
1	0	0	0	$-V_{DC}$	V_{DC}	$\frac{-V_{DC}}{3}$	$\frac{V_{DC}}{3}$	U_{240}
1	0	1	V_{DC}	$-V_{DC}$	0	$\frac{-V_{DC}}{3}$	$\frac{V_{DC}}{3}$	U_{300}
1	1	1	0	0	0	0	0	$O(111)$

Table 2.2: SVM Inverter States

6. The 3-phase output voltage is generated using the space vector modulation.

   Traditionally, the signals can be transformed back to the a-b-c reference frame using the inverse Clarke transform and applying those to PWM modules. These inverse Clarke transform equations are the following:

$$V_a = V_\alpha \tag{2.11}$$

$$V_b = \frac{-V_\alpha + \sqrt{3} * V_\beta}{2} \tag{2.12}$$

$$V_c = \frac{-V_\alpha - \sqrt{3} * V_\beta}{2} \tag{2.13}$$

   Another way to do this, which offers several advantages, is Space Vector Modulation (SVM). This technique incorporates the inverse Clarke transform in a slightly different way. Space vector modulation can present more stable output voltages, less harmonic distortion, simple hardware and flexible control[13].

   The process works as follows. The inverter has three outputs and can be only connected to two levels, the positive bus or the negative bus. Therefore it exists in only $2^3 = 8$ states at once, see Table 2.2

   The two cases where all the outputs are either connected to the positive or negative bus are called the null states as there is no line-to-line voltage between phases. All the states can be plotted in a so called SVM star, with a 60 degree angle between vectors and the null states plotted at the origin, see Figure 2.18.

   The process of SVM consists of three steps:

   (a) Sector identification

   (b) Space Voltage Vector decomposition into directions of sector base vectors U_{xxx} and X_{x+60}

   (c) PWM Duty cycle calculation.

   Using SVM, any resultant vector can be produced by combining two adjacent vectors for a specific time. In Figure 2.18 U_s is the resultant vector. This vector can be made by using the vectors U_{60} and U_0. During a PWM period T, U_0 is turned on for a time T_0/T and U_{60} for a time T_{60}/T. By modulating between adjacent base vectors, a vector of any angle can be produced. By modulating between the base vectors and the null vector also the magnitude of the resultant vector can be controlled.

   The duty cycles are computed through the following expressions.

$$T = T_0 + T_{60} + T_{null} \tag{2.14}$$

$$TU_s = T_0U_0 + T_{60}U_{60} + T_{null}O_{000} \tag{2.15}$$

   By decomposing these equations into the directions of their base vectors, the following expressions for the duty cycles are obtained:

$$T_0 = \frac{|U_s|}{|U_0|}T \tag{2.16}$$

$$T_{60} = \frac{|U_s|}{|U_{60}|}T \tag{2.17}$$

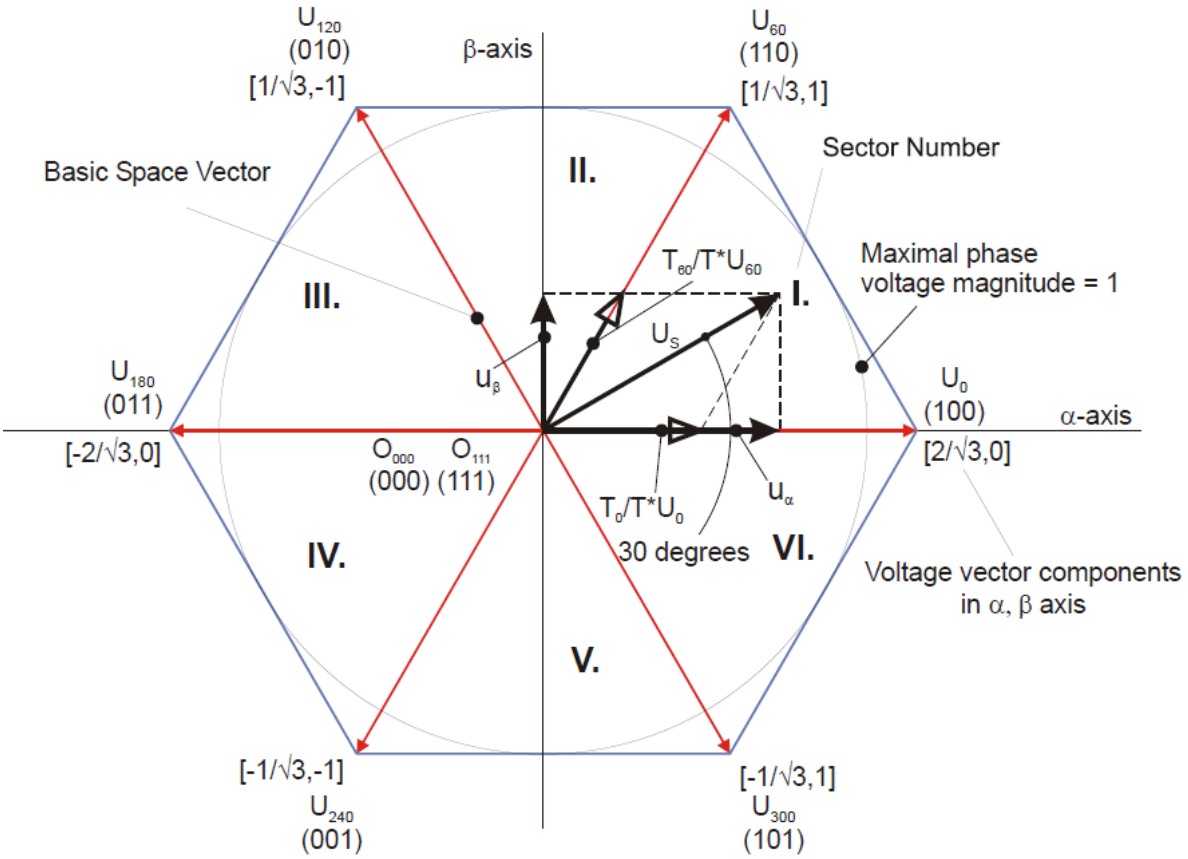

Figure 2.18: SVM Voltage Vectors [12]

3

MOTOR ANALYSIS

3.1. MODEL

Essential for motor control is a good understanding of the motor fundamentals. AC motors come in all shapes and sizes, have different working principles and can be constructed from different materials. All these influence the fundamental electrical and magnetic parameters of the motor. Usually these parameters can be measured by running tests on the motor.

In the Nuna case however this is not that straightforward. From the start of the project, the current motor was not present as it was still in transit from Australia back to the Netherlands. Initially it was thought the motor would return in the second half of December. Shortly after it became clear that the motor would not make its way back until the end of the project.

Therefore it was decided that a simulation model would be built so that some first characteristics could be found. The need for this was amplified by the lack of extensive information in the Mitsuba datasheets. After verification, this model can be used to simulate the motor with different winding distributions and different magnets. These results can be compared with the simulation results of the current setup of the motor to find out what are the most efficient motor configurations and which motor can deliver most torque.

Certain parameters are important to consider, especially the flux density in the motor and the fundamental motor parameters. It was quickly decided that a Finite Element Analysis (FEA) would suit the purpose. FEA is a commonly used technique in engineering to find an approximate solution to complex engineering problems in design. It takes away the need of doing physical tests, so it fits the requirements.

There are a lot of software packages and tools available which implement a finite element analysis for magnetics problems. Unfortunately, most of the more advanced tools come with a hefty price-tag. Then also it is necessary to decide whether a 2D or 3D analysis needs to be done. A 3D analysis generally takes more boundary effects into account and therefore should give the most accurate results. However, running these simulations takes a lot of computing power and its simulation will take a lot of time. One other plus in working with 3D methods, is that the already present CAD models can be used. These models are very precise and take away the need to convert a 3D model to a 2D plane. A huge drawback of this is the steep learning curve working with 3D packages, like Comsol and Ansys Maxwell. Since there was little experience in the group in working with FEA packages, the decision was made to use a 2D simulation. 2D analysis can also provide valuable insights in a much faster time, so more iterations can be done to approach reality as much as possible. The symmetry in the motors also makes it easier to convert to a 2D plane.

From all the possible 2D software options, FEMM [14]was chosen. It had certain key features that were favorable:

- It provided the possibility of visualizing the magnetic flux in the motor.
- It is relatively quick to learn.
- There is no need for a licence, so it is available for free online.
- It can be run through Matlab, a program with which the group had considerable experience and in which the control simulation is done.

In FEMM a model has been built from which the fundamental motor parameters can be deduced to be used in the Field Oriented Control algorithm. Also the flux density can be visualized in a very clear way and the back EMF can be calculated even though FEMM is inherently a static application.

3.1.1. MITSUBA

The Mitsuba M2096D-motor is a radial flux outrunner, which means that the rotor rotates around the stator. A big advantage compared to an inrunner lies with the air gap surface, which is substantially larger with an outrunner than with an inrunner. So the area through which the field lines pass is larger in an outrunner. This air gap surface determines the maximum achievable torque level and since this area is larger compared with an inrunner, the torque level will be higher in an outrunner.
The specifications provided by Mitsuba can be found in Table 3.1. Since the knowledge about this motor was limited, the AE group analyzed the motor for the Nuon Solar Team[15]. The dimensions and material properties found by them are listed in respectively Table 3.2 and Table 3.3. More specifications or dimensions are not known at this moment.
The connections of the windings are not clear as well, so for this thesis it is assumed that the motor is wye connected, because in a wye configuration a factor 1.7 less windings are needed for the same power as a delta connected motor. Besides, the current drawn from the battery at start-up is much lower for wye connected motors compared with delta-connected motors. These considerations seemed beneficial for a solar car.

Table 3.1: Specifications assembled Mitsuba motor

Motor specifications Mitsuba	
Diameter motor	262 mm
Length motor	73 mm
Number of pole pairs	16
Weight	11 kg
Nominal power	2.0 kW
Maximum power	5.0 kW (depends on the voltage of the battery)
Nominal load rotation speed	810 rpm

Table 3.2: Dimensions of the Mitsuba motor

Motor part	**Dimension**	**Parameter**	**Value**
Stator	axial length steel		40 mm
	inner diameter		180 mm
	outer diameter		240 mm
Rotor	inner diameter magnets		244 mm
	inner diameter back iron		249 mm
	outer diameter back iron		260 mm
Air gap	width	d_{air}	2 mm
Slots	number		36
	depth	d_s	19.5 mm
	width tooth	w_t	6 mm
	angle between slots	θ_s	12°
	opening width	w_{open}	3.8 mm
	Length tooth tip	$l_t t$	18.2 mm
Magnets	number		32
	angle between magnets	θ_m	11.25°
	width	d_m	3 mm
Windings	number per tooth		30
	thickness wire including isolation		1.6 mm

In Figure 3.1 a cross section of the motor is shown. The dimensions in this figure are also listed in Table 3.2. A more detailed section of the motor can be found in Figure 3.2, this also shows the dimensions of the isolation. These isolation materials were not taken into account for the simulation, because the properties

of these materials are not known and the boundary conditions of the simulations make the simulation more complex. This is not necessary for the purpose of this thesis.

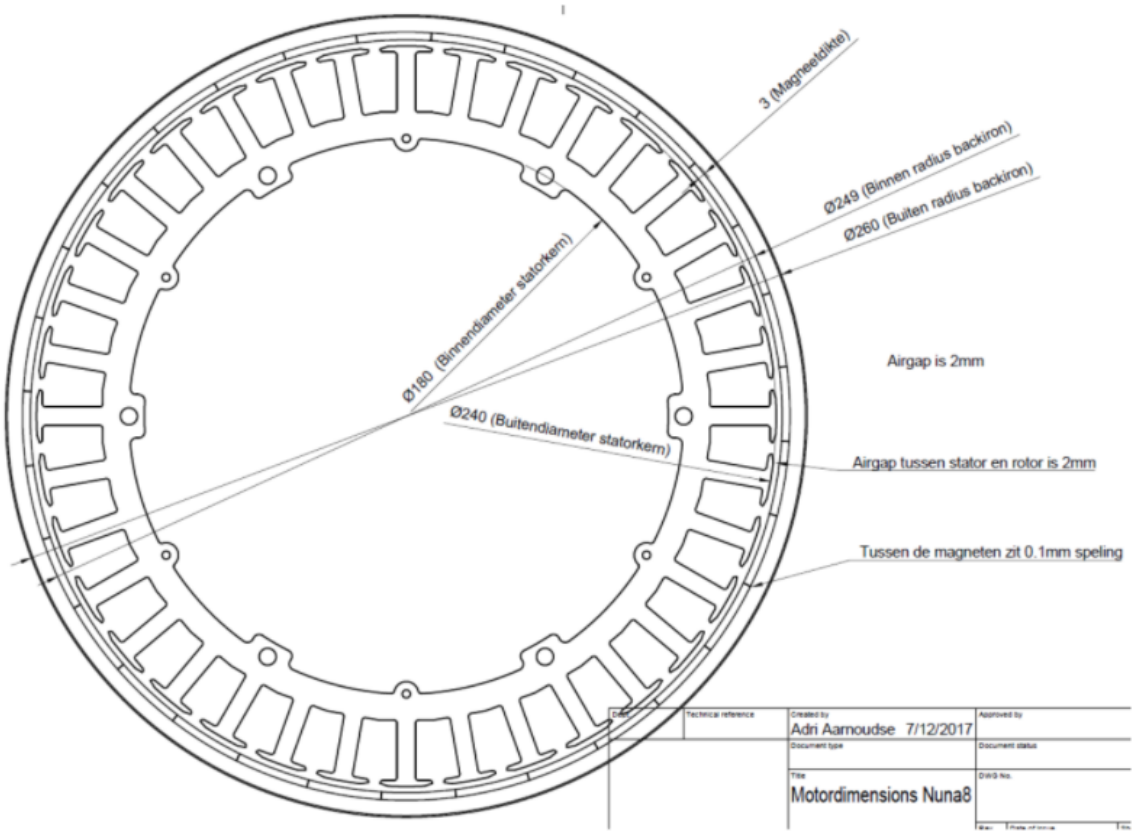

Figure 3.1: Dimensions of Mitsuba motor[15]

With these dimensions the motor is modeled in FEMM. The model is simplified, the teeth are less detailed for example. This makes the simulation less reliable, but for the purpose of this thesis the obtained parameters will be compared with the obtained parameters from other configurations of the same motor model, so the results of the simulations can still be compared with each other. A little section of the model modeled in FEMM is shown in Figure 3.3. The parameters of this model can be found in Table 3.2.

The materials of the motor are unknown. For some materials, like the magnets, the material properties have been simulated and tested by the AE group [15] to make an estimation of what materials the motor consist of. The properties of the materials taken for the FEMM simulation are obtained from these estimations and are listed in Table 3.3 and the properties of these materials can be found in Figure D.1a. These are the properties inserted in FEMM.

Table 3.3: Materials used for the FEMM simulation

Motor part	**Material**
Back iron	pure iron, annealed
Stator	steel
Magnets	N38UH
Wire	Copper 30 AWG

The magnets need to be magnetized radially. So every second magnet points to the center and the other magnets point outwards. It is unknown if these magnets are magnetized radial or parallel, so the assumption is that the magnets are magnetized parallel, because that is easier to produce.

To model the windings, three different circuits with the same material properties where made, one for each phase and they are called, 'A', 'B' and 'C'. The current through these currents can be set using Matlab. When

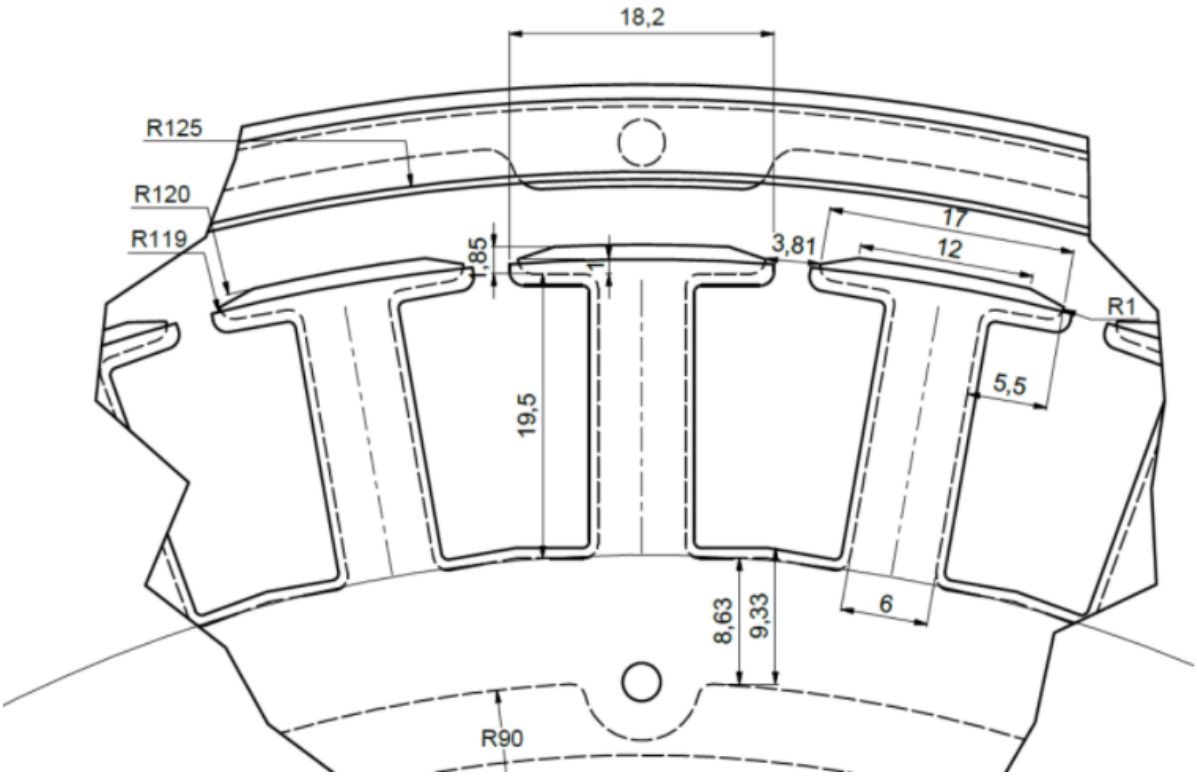

Figure 3.2: Dimensions of Mitsuba motor[15]

assigning these circuits to the dedicated parts, the direction of the current can be indicated using a + or - sign and the 'number of turns' of the block properties can be set to the desired number of turns. A more detailed section of the FEMM model is shown in Figure 3.4. The arrows in the magnets represent the magnetization of the magnets. The information between brackets describes the circuit the block is assigned to and the number of turns.

WINDING PATTERNS

Part of this research is to find out if the Mitsuba motor can be made more efficient, while having a similar or higher torque. One way to do so is to investigate the winding configuration. At the moment, this winding pattern is concentrated, which means that every slot has the same number of turns. The layout of the current configuration is shown in Table 3.5. The three phases are indicated with A, B, C and the + or - sign indicate the direction of the current.
The parameters of this set-up are $k_w = 0.945, q =, 3/10$ [16].

When using the motor with a sinusoidal back-EMF it is more efficient to have a distributed winding pattern. Another possible pattern is shown in Figure 3.6 [8].

The windings of one phase are normally connected in series. The wires that are not wound around teeth, but are part of the circuit, this includes the connections between the phases and the connection with the controller, are called the end-windings. The can have a significant effect on the phase resistance and phase inductance depending on how the stator is wound. Unfortunately, it is impossible to simulate them in a 2D finite element analysis, so these should be taken into account when the simulation results are evaluated.

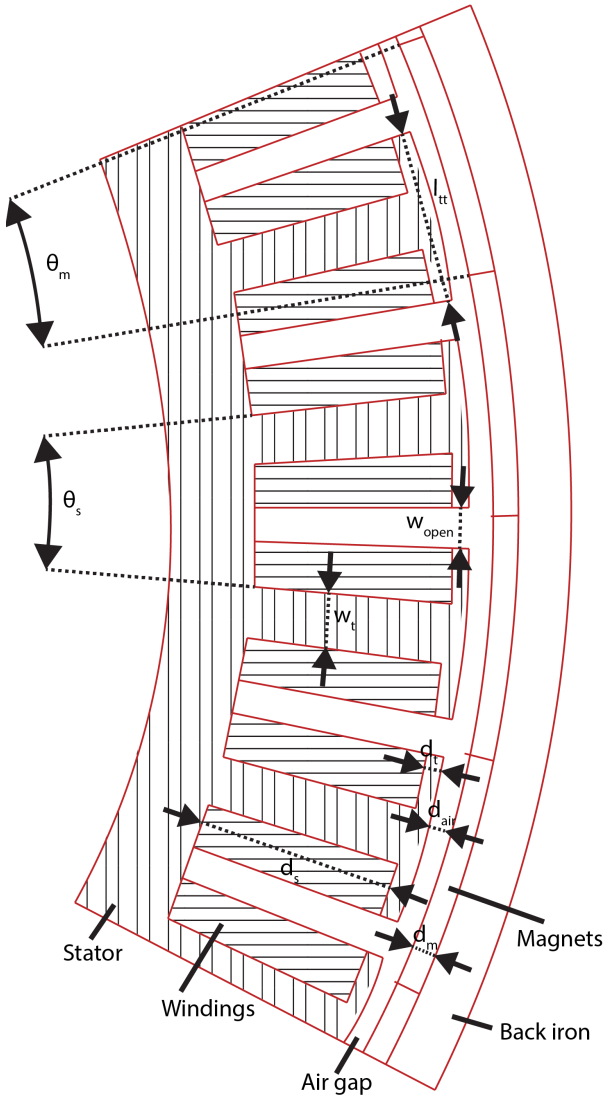

Figure 3.3: Dimensions of the FEMM model

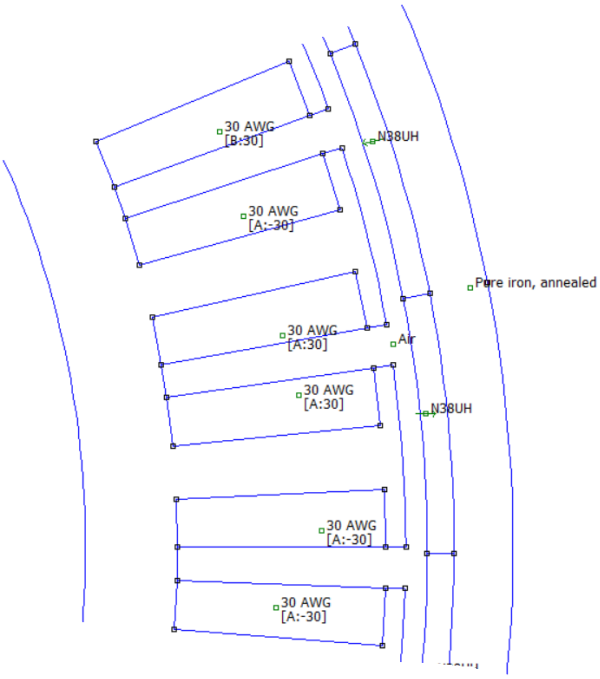

Figure 3.4: Detail of the FEMM model of the Mitsuba motor with material properties

C-	A+	A-	A-	A+	A+	A-	B+	B-	B-	B+	B+	B-	C+	C-	C-	C+	C+

Figure 3.5: Winding pattern A, current winding pattern, repeated four times

A+	A-	B-	B+	B-	B+	C+	C-	A-	A+	A-	A+	B+	B-	C-	C+	C-	C+

Figure 3.6: Winding pattern B, is repeated two times

3.1.2. MARAND

The former Nuna motor is the Marand, a motor specially designed for solar car applications. It is an axial flux motor, which means the field across the air gap is in the axial direction rather than in a radial direction. The motor consists of two outrunner rotor rings, which contain the permanent magnets and one stator in between. See Figure 3.7.

The stator is coreless, meaning there is no conductor around which the windings are wrapped. This removes weight, core losses and the effects of cogging torque. Cogging torque is torque produced produced by the magnetic attraction of the stator and rotor and is a large cause of torque ripples. Coreless motors however often suffer from lower field strengths, due to fact the a steel core helps drive current in the windings in the air gap, and there is less winding space. These factors all limit the output torque of the motor.

Each rotor magnet ring consists of 40 neodymium-iron-boron rare earth magnets. This gives a total of 80 magnets per motor.

The stator is wound of around 40 metres of Litz wire across the three phases. Litz wire is a multi strand wire and the wire used has approximately 340 strands per wire. Litz wire is used to reduce the skin effect of the wire, the impact on the wire impedance to high frequency current. Litz wire uses the full cross sectional area to carry current due to the individual strands being thinner than the skin depth.

The stator has 6 windings for 3 phases, allowing for series or parallel wiring. Each phase is repeated 40 times. There are 3 phases in the width of a single magnet. See Figure 3.8.

The axial nature of the motor creates a problem with modeling the motor in FEMM. As FEMM is a 2D program it is unfortunately not possible to draw both accurate dimensions and depth. Because the flux is in the axial direction, it would make no sense to make a radial 2D intersection. To circumvent this problem, the motor is rolled out and linearized. Next to that it is cut off at the periodic bounds.

There are some inaccuracies with this FEMM 2D method. The first is concerned with non linearity prop-

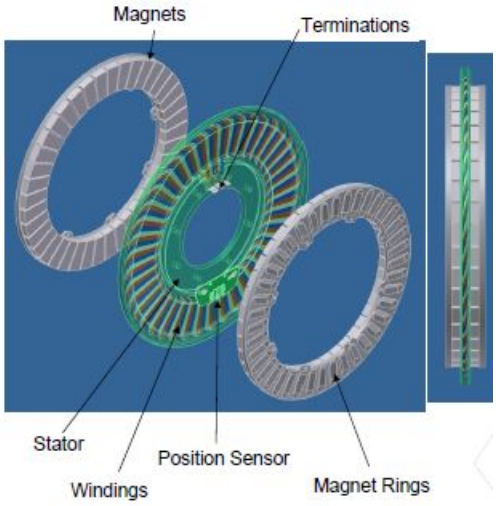

Figure 3.7: Intersection of the Marand motor[17]

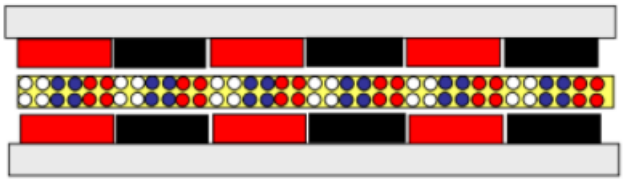

Figure 3.8: Linearization Marand Stator

erties of magnetic materials. This could cause different saturation levels in the different radii of the magnetic cores. Another concern can occur when certain dimensions are not proportional in the radial direction. These dimensions do not translate well and therefore introduce inaccuracies[18].

However for this particular motor, there is no magnetic core so those non linear properties need not to be taken into account. Also problems with non proportional dimension in the radial direction, tend to happen with the teeth of a stator, which may come in various shapes. The Marand does not have teeth on its stator, so problems regarding this aspect are expected to be minimal.

The model is then built as can be seen in Figure 3.9. First the proper geometry has to be imported. This can be done by importing a 2D DFX file or by hand drawing, the latter which is the case here as there are no 2D DFX files available. Every material needs to be a closed block so that it can be assigned a block label. This block label is used by the program to define the material properties.

For the magnets, neodymium-iron-boron magnets are used. The rotor back iron is made up out of 416 stainless steel, which falls in the 41xx category (Society Automative Engineers Standard), the same category steel grade as the actual SCM (Japanse Industry Standard) grade steel, which is a Chromium-Molybdenum alloy. The stator is made of copper wire of appropriate thickness and the rest is assigned the air label. As the stator is coreless, there is no magnetic coupling between the stator and rotor and the stator is said to be magnetically independent. This means that the windings should not alter the magnetic flux path and this means not all windings have to modeled to get an accurate result[19]. This hugely decreases simulation times as less blocks mean less mesh elements, which results in less calculations to be made by the program.

As this intersection of the Marand motor has no complete boundaries all around, a boundary needs to be defined for the problem to give a solution and not be stuck in endless calculations. This boundary can be seen at the edges of Figure 3.9.

To gain an understanding of the back EMF shape and motor constant, two analyses will be done, a static and a dynamic.

The static analysis will provide a deeper insight in the flux distribution of the motor, which can be used to derive the motor constant. Using the flux distribution, the FEA solver can implement a Maxwell stress tensor, a method used in classical electromagnetism to represent the interaction between electromagnetic forces

Table 3.4: Dimensions of the Marand motor

Rotor	inner radius	113.8 mm
	outer radius	157.5 mm
Air gap between assemblies	width	10.9 mm
Air gap to stator	width	1.75 mm
Slots	number	Slotless
Magnets	number	2x 40
	width (magnets+gap)	21.31 mm
Windings	number per phase	4
	thickness including isolation	3.7 mm

Table 3.5: Materials used for the FEMM simulation

Component	**Marand**	**FEMM**
Back iron	SCM grade steel	416 Stainless Steel
Stator	Coreless	Coreless
Magnets	NdFeB	NdFeB
Wire	Copper Litz Wire	Copper AWG 7 (stranded)

and mechanical momentum. This tensor calculates the torque. Knowing the current, one can estimate the torque constant.

To get more insight in the actual shape of the back EMF signal and approach the motor constant better, also a dynamic analysis will be done.

In this analysis a group of windings is iterated through the motor and records the important parameters like flux density, vector potential and flux linkage with respect to the initial mesh elements. Using these values from different positions, different calculations and plots can be made, like the back EMF waveshape. FEMM is inherently a static analysis, so some code needs to be written to loop the windings to a new position and records the values. This code can be found in Appendix B.

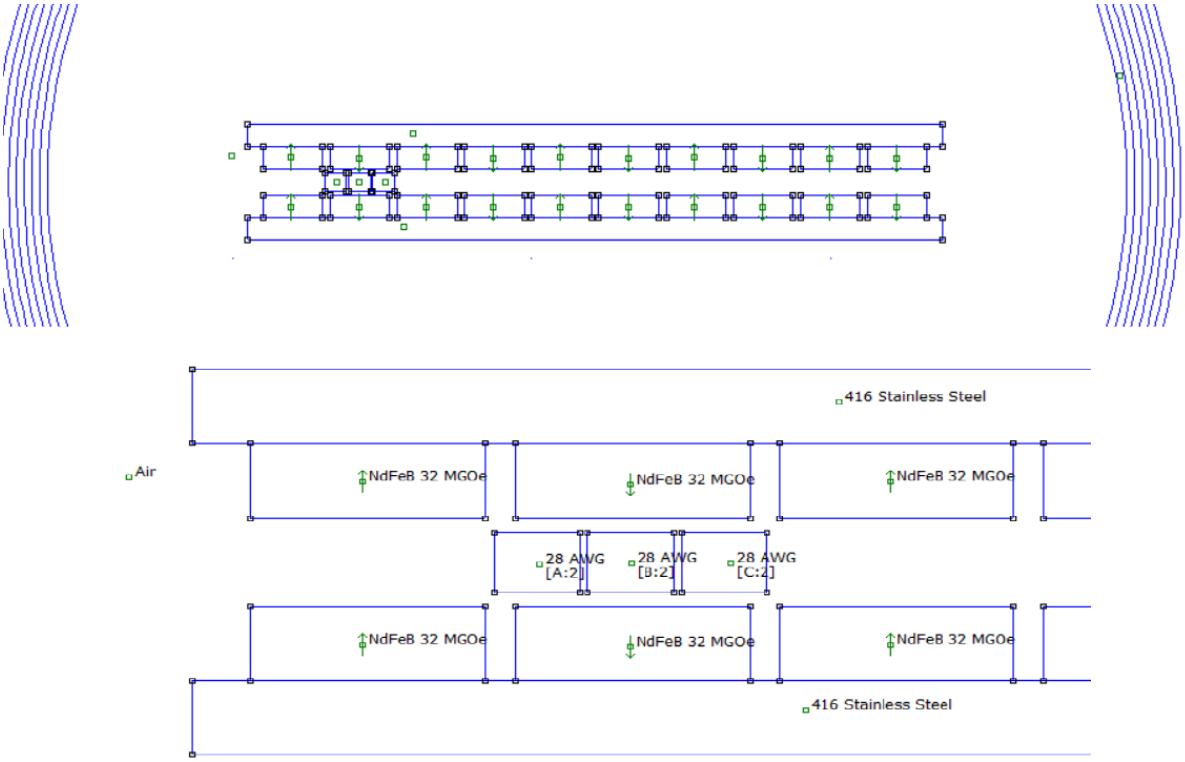

Figure 3.9: Marand Preprocessing Model

Motor Specifications	
Number of poles	40
Number of phases	3
Mass of wheel motor	15.4 kg
Nominal speed	111 rad/s
Nominal torque	16.2 Nm
Phase resistance	0.0575
EMF constant – L-N RMS EMF/speed	0.45 Vs/rad
Torque constant per phase	0.44 Nm/A

Table 3.6: Caption

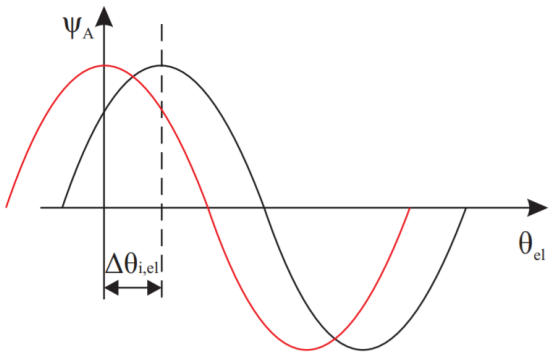

Figure 3.10: Current and desired flux linkage phase A[20]

3.2. RESULTS

3.2.1. MITSUBA

First the motor is modeled with the winding configurations shown in Figure 3.5, this is the winding pattern that is currently wound on thee motor. To simulate the inductance and the back EMF, θ, the angle between the d-axis of the rotor and the starting position of the electric period, should be 0, because this is not taken into account during the modeling of the model. So first, this starting point needs to be defined. The starting position is defined at the maximum magnetic flux linkage of the phase A. This is illustrated in Figure 3.10.

Resistance The phase resistance R_{ph} of the motor cannot be determined from the simulation. It is approximated by Formula 3.1, where ρ is the resistivity of the wire, in this case copper, l is the length of the series turns and A is the conductor cross section.

$$R_{ph} = \frac{\rho l}{A} \tag{3.1}$$

The resistivity of copper is $1.7 \cdot 10^{-8} \Omega m$. The wire is round and has a diameter of 1.6 mm including isolation. So A is $0.8^2\pi = 2.01 mm^2$ including isolation.
The length of a tooth is 6 mm and the depth is 40 mm. The wires are wound in three layers; 11 windings on the bottom layer, 10 on the second and 9 on top. The length of one winding on the bottom layer is approximately 95 mm. On the second layer it is approximately 98 mm and on the top layer 101 mm. The length of wire around one tooth is then 2934 mm. Per phase it is wound around 12 teeth with approximately 47 mm in between. This gives us a length of $12 \cdot 2934 mm + 4 \cdot 47 mm = 35.4 m$ wire. When using these dimensions the phase resistance calculated with equation 3.1 is $299 m\Omega$.

Magnetic Flux The FEMM simulation gives the flux distribution after analyzing the motor model. For the Mitsuba motor a detail of this distribution is shown in Figure 3.11. The field lines loops through the magnets and back iron are clearly visible and the different currents through the different windings induce visible difference in the flux lines.

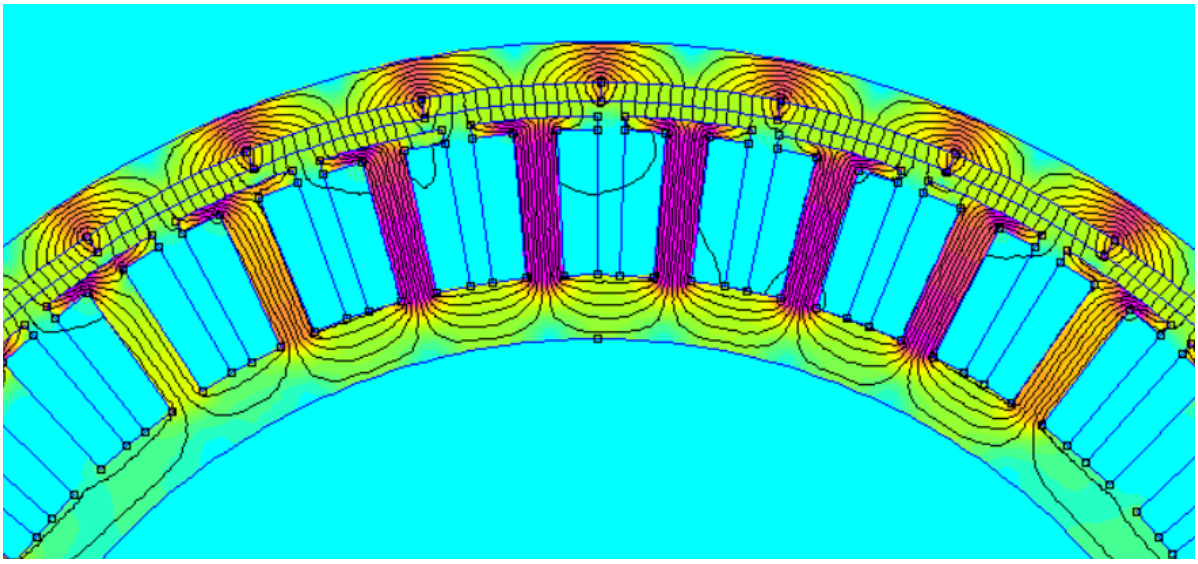

Figure 3.11: Flux density of the Mitsuba motor in current configuration

Inductance The synchronous inductances of surface mounted PMSMs are almost equal, because the permanent magnets are surface mounted and reluctance is the same in every position, which means that $L_q \approx L_d$, that are the inductances corresponding with currents respectively I_d and I_q. This can be calculated with equation 3.2 if the rotor is locked to phase A, which means $\theta_{el} = 0$.

$$L_d = \frac{2}{3}L \tag{3.2}$$

To calculate L_d phase A will be connected to the positive potential, while B and C are connected to ground, the simulation will calculate the flux linkage of phase A λ_L. Next B and C will be connected to the positive potential and A to ground and the simulation will again calculate the flux linkage of phase A λ_M. The inductance is calculated with Equation 3.3.

$$L = \frac{\lambda_L - \lambda_M}{I_A} \tag{3.3}$$

The rotor is aligned to the place where the flux linkage of phase A is highest. With a current of $I_a = 20A$, the flux linkage $\lambda_L = 0.1525Wb$ and $\lambda_M = 0.1206Wb$, so $L = 1.6mH$ and $L_d = L_q = 1.1mH$.

Back-EMF The back-EMF for phase A can be calculated by using Equation 3.4.

$$E = \frac{d\lambda}{dt} = \frac{d\lambda_a}{d\theta_e}\frac{d\theta_e}{dt} = \frac{d\lambda_a}{d\theta_e}\omega_e, \tag{3.4}$$

where E is the back-EMF, λ_a is the flux linkage of phase A which can directly be obtained by the FEMM analysis, θ_e is the electrical degree and ω_e is the electrical angular speed. The electrical angular speed is linked with the mechanical angular speed in the following way: $\omega_e = p\omega_m$. Since the results obtained from FEMM are discrete, this derivative can be written as a discrete derivative:

$$\left(\frac{d\lambda_a}{d\theta_e}\right)_i = \frac{\lambda_{a,i} - \lambda_{a,i-1}}{\Delta\theta_e}, \tag{3.5}$$

The back-EMF constant k_e is calculated with Formula 3.6.

$$k_e = \frac{E}{\omega_e} \tag{3.6}$$

The simulation is done with $I_d = 20A$ and $I_q = 0A$. The back-EMF is plotted in figure 3.12 and the calculated back-EMF constant k_e is 0.9273.

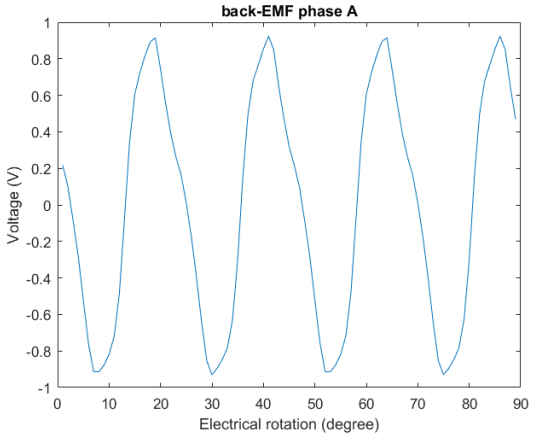

Figure 3.12: Back-EMF of phase A of the Mitsuba motor in current configuration

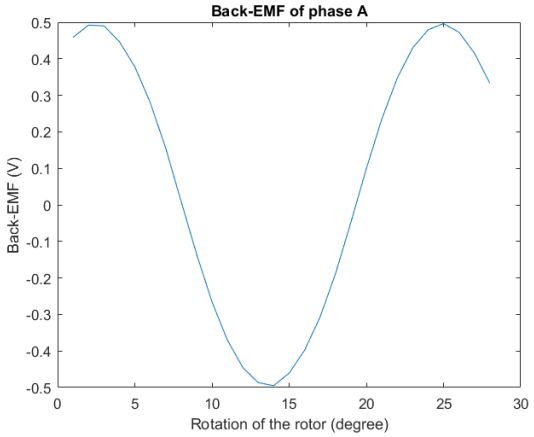

Figure 3.13: Back-EMF of the Mitsuba motor with winding pattern 2 3.6

WINDING B

Secondly, the simulations are done with another winding pattern, the pattern shown in figure 3.6. The number of windings per slot stays the same, to make sure the motor will not become thicker as a result of more windings.

Resistance The number of turns per coil stays the same, but the windings are only wound around alternating teeth. So the total length of the wire around the teeth halved and the end-windings stay the same, this gives a length of $6 \cdot 2934mm + 4 \cdot 47mm = 17.8m$. Assuming the same wire will be used as in the current configuration, the resistance is $151m\Omega$.

Back-EMF The back-EMF is plotted in figure 3.13. The back-EMF is a much smoother sinusoidal. The back-EMF constant k_e is 0.4966.

Inductance The inductance is calculated with equation 3.3. The phase current I_a is set to 20A. The corresponding flux linkage is $\lambda_L = 0.0834Wb$ and after grounding phase A and connecting phase B and C, the flux linkage $\lambda_M = 0.0436Wb$, by using equations 3.3 and 3.2 the calculated inductances are $L = 2mH$ and $L_d = L_q = 1.3mH$. However, the end-windings are not taken into consideration by the simulation software, so the inductance might be higher than calculated here.

3.2.2. MARAND

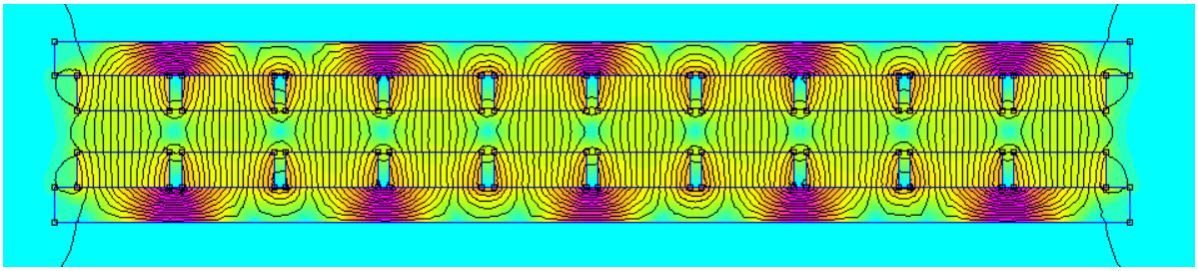

Figure 3.14: Flux Density Marand

MODEL

The following results come from simulation or calculation on the Marand motor.

Resistance Also in the case of the Marand the resistance cannot be calculated from the finite element analysis. Therefore a calculation is made from standard formula 3.1.

The resistivity of copper is $1.7 \cdot 10^{-8} \Omega m$, the wire length can be taken from the datasheet to be around 40 meters and the diameter of the wire can be calculated from air gap distances to be 3.7 mm. Putting these numbers in the formula, results in a resistance of 0.06Ω.

Magnetic Flux After doing one static analysis in FEMM, the flux distribution can be plotted a shown in Figure 3.14. It is very clear to see the various magnetic loops that exist between pole pairs and that the magnetic flux is the strongest when it runs in parallel with the rotor direction, exactly what is desired.

Another positive result is the fact that stator, being coreless, is indeed magnetically independent from the rotor. The presence of the windings does not alter the flux path in the air gap.

Inductances As in the case of the Mitsuba, because the motor contains Surface Mounted PM's, the inductances can be measured in similar fashion using the following formula:

$$L = \frac{\lambda_L - \lambda_M}{I_A} \tag{3.7}$$

The flux linkage is calculated when phase A is positive and phase B and C are connected to ground, and for the case when A is grounded and the other phases are positive at the point where the flux linkage is the highest for phase A. The inductance was then to be found at $L_d = 1.58 \mu H = L_q$.

Back EMF From the dynamic simulation, the motor constant can be calculated through the following formulas[19]:

$$E = \frac{d\lambda}{dt} = \frac{d\lambda}{d\theta_e}\frac{d\theta_e}{dt} = \frac{d\lambda}{d\theta_e} p\omega_m \tag{3.8}$$

$$k_e(\theta_e) = \frac{E}{\omega_m} = p\frac{d\lambda}{d\theta_e}, \tag{3.9}$$

where E is the back EMF, λ the flux linkage, θ_e the rotor electrical angle, k_e the motor constant and ω_m the mechanical velocity and p the number of pole pairs used to convert ω_m to electrical frequency.

HALBACH ARRAY

The Marand motor is also available with the permanent magnets arranged in a Halbach array. In the ideal case a the magnetization direction would continuously change with position, but this is not a reality. In practice a finite amount of magnets has to be used. An earlier version of the Marand motor (1997) employed 4 magnets per pole[21], so this is also assumed in the simulation.

This means that each magnet from the previous simulation will be split in 4 individual sections with different magnetization direction, which can be seen in Figure 3.16. The arrows already clearly indicate how the field lines will be guided through the motor.

Due to the focusing of the magnetic field, the distribution of flux has changed a lot. This can be seen in Figure 3.17 and more in detail in Figure 3.18. The flux component in the direction of motion is still high but

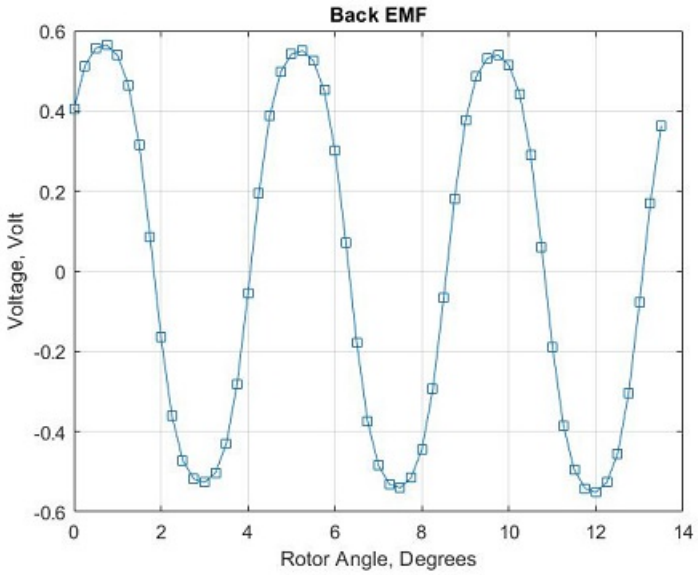

Figure 3.15: Back EMF waveform from FEMM simulation

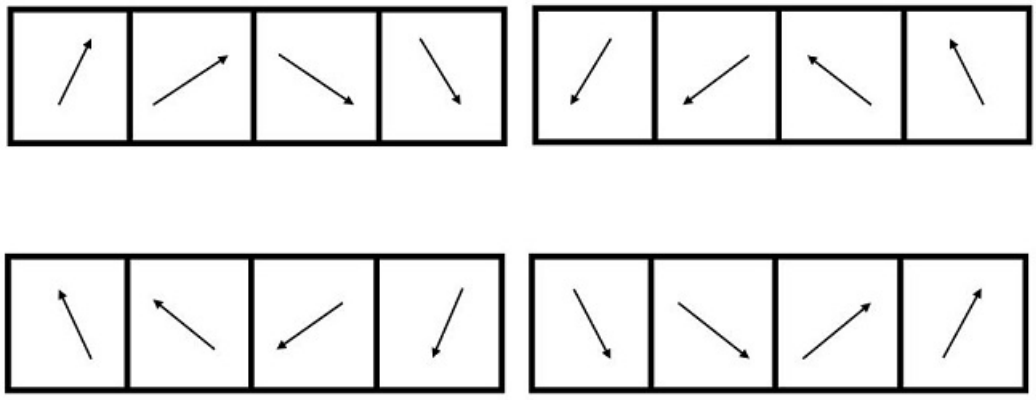

Figure 3.16: Employed Halbach Array

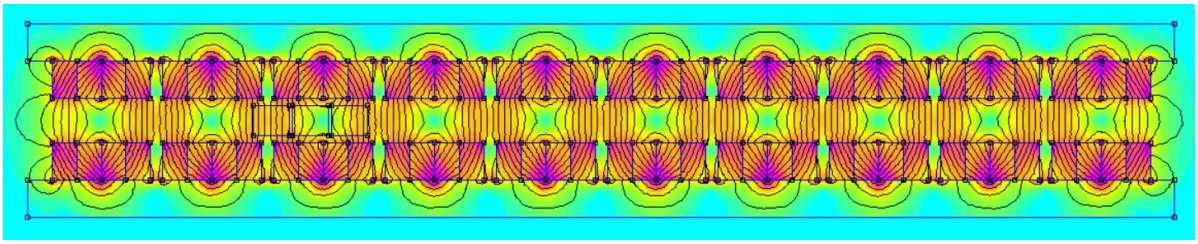

Figure 3.17: Flux Density Marand with Halbach Array

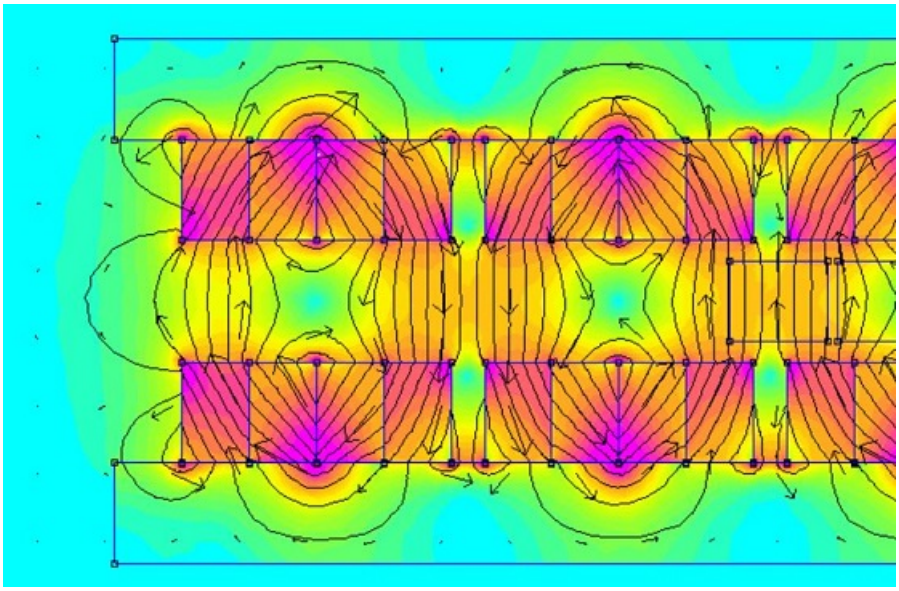

Figure 3.18: Detailed view of flux in Marand Motor with Halbach Array

much more evenly distributed. Also the flux through the air gap is much stronger than without Halbach array. Another important aspect of the Halbach array is the reduction of flux lines in the back iron. In normal configuration the back iron serves to guide the flux inside the motor to its opposite pole. With this Halbach array the back iron almost isn't necessary anymore. This means that a reduction in size is possible and therefore a reduction in weight. This weight reduction doubles as it applies for both rotors.

MEASUREMENT

The Marand motor was measured while mounted in the car. Using the TI C2000 Microcontroller Launchpad, being used by the other subgroup, the motor was initialized and the initial motor parameters were established. The phase resistance is $41.4m\Omega$ when the motor is still cold and $39.3m\Omega$ when the motor is warm.

The d- and q-inductances are almost equal, because the permanent magnets are surface mounted and reluctance is the same in every position.

$$\mu_{PM} \approx \mu_{air} \rightarrow L_d \approx L_q \tag{3.10}$$

The inductances $L_d = L_q = 0.17066\mu H$.

The back-EMF was measured in a different way. While mounted in the car the wheel was driven with a constant speed, supplied by a hand-drill.

The three phases of the motor were accessible and connected to a oscilloscope. See Figure 3.19.

As there were only 2 voltage probes available and the neutral point was not accessible, a one-phase line-to-line voltage was measured.

The back-EMF constant can then be calculated according to the following formula:

$$k_{e-ph} = \frac{V_{pk}}{\sqrt{3}\omega_{el}} = \frac{V_{pk-pk}}{2\sqrt{3}\omega_{el}} = \frac{V_{pk-pk}T_{el}}{2\sqrt{3}2\pi} \tag{3.11}$$

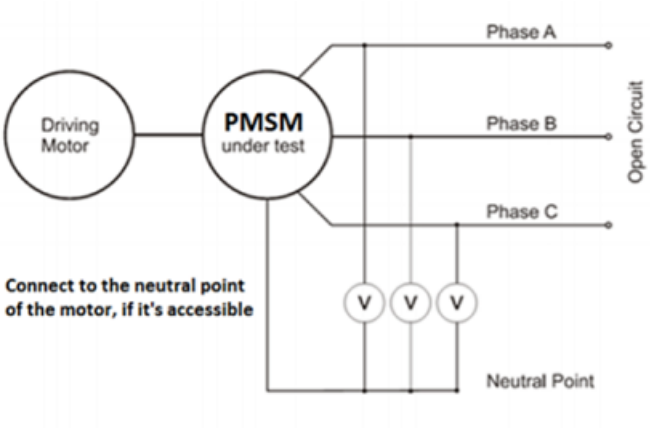

Figure 3.19: Test Setup[22]

Figure 3.20: Measurement signal of the Marand Back EMF

Figure 3.21: Measurement Back EMF

,where V_{pk-pk} is the peak-to-peak voltage of the back EMF wave, ω_{el} the electrical frequency, T_{el} the period and k_{e-ph} the motor constant for one phase. Using the results found in figure 3.20, which are $V_{pk-pk} = 8.9V$ and $T_{el} = \frac{1}{f_{el}} = \frac{1}{27.3972} = 0.0365s$, the back-EMF constant is found to be $k_{e-ph} = \frac{0.3248}{21.7656} = 0.02Vs/rad$

3.3. DISCUSSION

In table 3.7 the calculated and simulated parameters are put together. These parameters are not specified in the datasheets, so there is no comparison possible. The simulation with winding A can be verified with measurements of the current motor, when this motor will be available for measurements. Verification of simulation winding B is not possible.

Parameter	Datasheet	Simulation winding A	Simulation winding B
R_s	-	$299m\Omega$	$151m\Omega$
L_d, L_q	-	1.1 mH	1.3mH
k_e	-	0.9273	0.4966

Table 3.7: Comparison parameters of Mitsuba motor

Comparing the results of the Marand in Table 3.8, the following observations can be made. The resistance values are from all instances within reasonable range. The fact that the calculations provide a slightly higher value can be attributed to the roughness of the data to work with. If the wire is a little bit shorter than the indicated 40 metres than the result approaches the datasheet value already. The value in for the measurement still is noticeably lower.

The inductance has no value in the datasheet. But the recorded value from measurement and calculated from the FEMM model are in strong agreement.

The motor constant is a different story. Datasheet and model are in a reasonable range. The results can be improved by taking losses and boundary effects into account. Also with FEMM being a static program and the simulation being a dynamic one, some accuracy was always going to get lost. The motor constant value from

measurement seems to be a wrong one. This measurement was carried out with the intention to primarily see what the back EMF waveshape looked like. The actual value was calculated much later from the captured waveforms and the measurement was not repeated, because the most important feature was revealed and a value for the motor constant was already present in the datasheet. The error measurement is probably due to the connection between the oscilloscope voltage probe and the motor terminals, which were hard to clip together.

Parameter	**Datasheet**	**Model**	**Measurement**	**Halbach**
R_s	0.575Ω	0.063Ω	0.0414Ω	0.063Ω
L_d, L_q	-	$0.158\mu H$	$0.17\mu H$	-
k_e	$0.45Vs/rad$	$0.58Vs/rad$	$0.02Vs/rad(1-phase)$	$0.57Vs/rad$

Table 3.8: Comparison parameters of Marand motor

4

INVERTER

This chapter is about the inverter of the motor drive. First the theory about inverter topology, possible power devices and control methods is drawn up. Secondly, the wavesculptor 20, the predecessor of the current motor controller, is presented. Finally, some specifications and recommendations are given to connect a new inverter with the controller and motor.

4.1. THEORY

A variable frequency drive (VFD) is needed to adjust the speed of the motor. This drive contains the inverter and the software that controls the inverter. Since the motor is a three-phase motor, the inverter also needs to be a three-phase inverter. The interest in variable frequency drives starts growing again now that electric vehicles are becoming a more familiar part of our daily life.

4.1.1. TOPOLOGY

The most simple configurations of a three-phase inverter is shown in figure 4.1. However, a lot of topologies exist for the inverter.

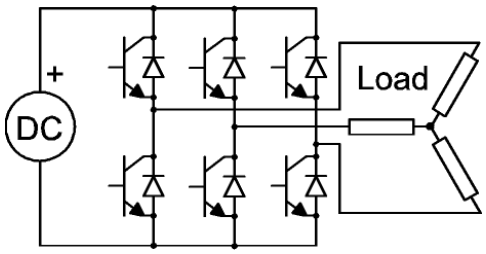

Figure 4.1: Three-phase inverter with IGBTs

Voltage source inverter In Figure 4.2 a voltage source inverter (VSI) is shown. This type of inverter is widely used in electric vehicles, because the source of an electric car is a voltage source (ie. a battery). There are some drawbacks to this type of converter, the peak AC line-to-line voltage cannot exceed the DC bus voltage, so sometimes a boost converter is needed. The volume of the capacitor bank could be more than 30% of the whole inverter, which makes it heavy. The power devices on one leg cannot be switched on simultaneously, so depending on the devices the dead time between two switches can become high, that may result in higher torque ripples.

Current source inverter A current source inverter (CSI), as shown in Figure 4.3 is a boost-type inverter, so the output voltage is higher than the bus voltage. The capacitors before the motor filter the pulse current produced by the switches, so a smooth sinusoidal output can be obtained. The diodes in series with the switching devices are needed to block bidirectional voltages. To capture the energy produced by regenerative

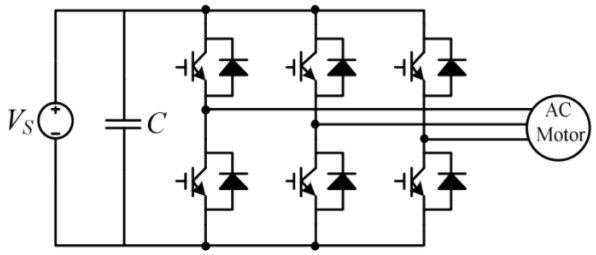

Figure 4.2: Voltage source inverter

breaking, a DC-DC-converter is needed after the battery. This type of inverter has some advantages over voltage source inverters. For example, the motor can run on a higher speed with the same input voltage compared to a VSI, because the AC voltage is higher than the DC bus voltage. Higher power density can be realized by a CSI, because this type doesn't need big capacitors on the DC side. However, the power efficiency is lower than that of the VSI, because of the losses in the diodes.

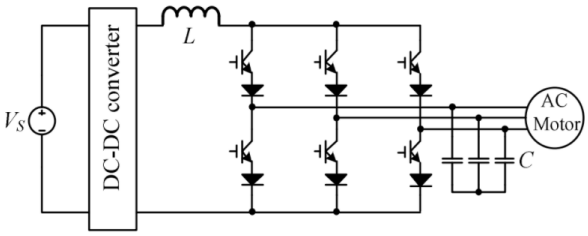

Figure 4.3: Current source inverter

Z-source inverter A Z-source inverter, as shown in Figure 4.4 combines a Z-source circuit with a conventional inverter. This inverter is a buck-boost type inverter. This topology is more reliable than the topology of a VSI or CSI, because the shoot-through state, where both switching devices on one leg are on simultaneously, is allowed, this produces a short voltage boost. However, the power efficiency is lower than the VSI.

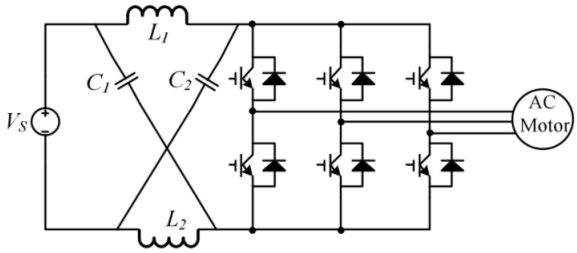

Figure 4.4: Z-source inverter

Soft switching inverter All of the above are hard switching inverter, another type of inverter is the soft switching inverter. This is a voltage source inverter with an extra circuit in front of it, as shown in figure 4.5. This extra circuit brings down the switch voltage of the voltage source inverter to zero before the gate voltage is applied. This type of inverter reduces the power losses. In Lai et al. [23] the operating principle is explained in more detail. The efficiency can be approved with this type of inverter, but the reliability will decrease as a result of more power switching devices. And the control of this type of inverter is more complex than for a hard-switching inverter [24].

Aside from the topologies explained above, more complex topologies exist, like multilevel inverters [25].

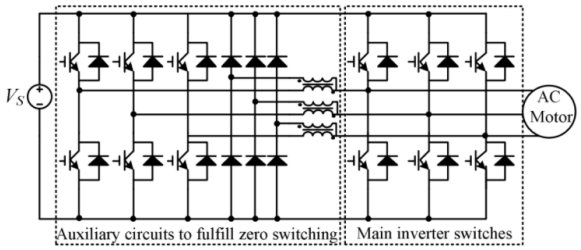

Figure 4.5: Soft switching inverter

The output of the inverter contains harmonics. This has some undesirable effects, like output waveforms that are not pure sinusoidal, degradation of components and torque ripple. Inverters used for AC motor drive applications are expected to have less low order harmonics in the output voltage waveform, because higher order harmonic voltage distortions are, in most AC motor loads, filtered away by the inductive nature of the load itself. Harmonic reduction can be achieved by either filtering, selected harmonic reduction chopping or pulse-width modulation [26].

4.1.2. POWER DEVICES

The switching elements of the inverter are power semiconductor devices. A lot of these devices exist, but only two of them are meet the requirements of this application, namely the insulated-gate bipolar transistor (IGBT) and the Metal-Oxide-Semiconductor Field-Effect Transistor (MOSFET). In Figure 4.6 the working regions of these devices can be found.

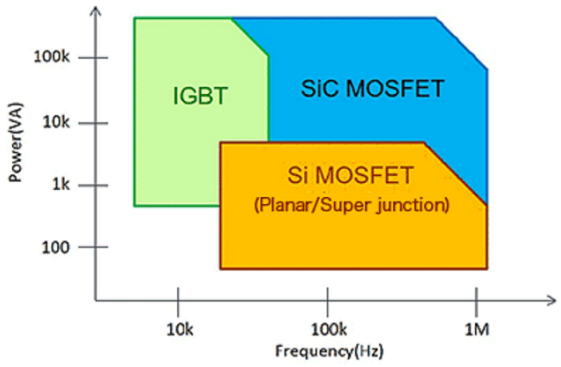

Figure 4.6: Power devices split up by frequency and voltage characteristics[27]

IGBTs An IGBT is a voltage controlled power device. When the breakdown voltage of the inverter is above 1 kV normally a IGBT is used. The IGBT combines the simple gate-drive characteristics of MOSFETs with the high-current and low-saturation-voltage capability of bipolar transistors. An IGBT cannot conduct current in the opposite direction, so an additional diode is placed in parallel, because in this bridge construction reverse current is needed. Especially for lower voltages (under 1 kV) these diodes introduce extra losses.

power MOSFETs For lower voltage ratings or high frequencies (over 50kHz) normally power MOSFETs are used. The injection of minority carriers take less time during turn-on and turn-off, so the maximum switching frequency is higher.
Traditionally, these devices are made from silicon or silicon carbide. Lately, a lot more research has been done on gallium nitride MOSFETs. These devices have up to 20% less losses and have a higher maximum switching frequency compared to Si- or SiC-MOSFETs. However, they are fragile and may not be robust enough to drive a car for through the dessert of Australia[28].

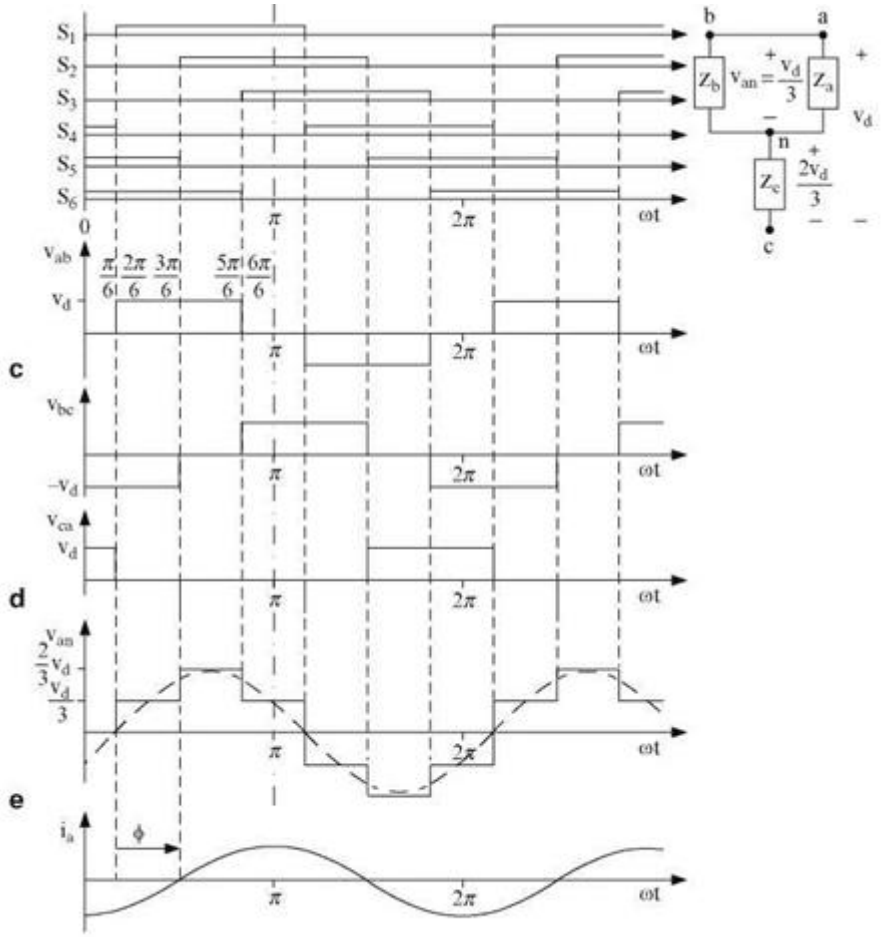

Fig. 5.48 (c) 6-pulse, voltage-source inverter with wave forms at time $t = t_3 = \frac{6\pi}{6\omega}$, where phases

Figure 4.7: Gate signals and output signals of stepped wave inverter

4.1.3. CONTROL METHODS

The inverter can either control the motor with a stepped wave or with pulse width modulation.

Stepped wave When controlled by a stepped wave, the switching devices are switched in a sequence with a difference of T/6 and a duration of T/2, where T is the duration of one cycle. The gate signals and output signals of this type of inverter is shown in Figure 4.7. The main drawback of this type of control is large harmonics at low frequencies in the output voltage.

Pulse width modulation Another implementation of the inverter is with pulse width modulation (PWM). The gates are controlled with pulses. When using single PWM, only one pulse per half cycle controls the output voltage, varying the width of this one pulse changes the output voltage. When using multiple or sinusoidal PWM multiple pulses per half-cycle, the width of the pulses is adjusted to for a sinusoidal output. This method is easier to implement and control with today's microprocessors. However, the switching frequency increases drastically and thereby also the losses and degradation of those components.

4.2. NUNA INVERTERS

The motor is controlled by the Tritium WaveSculptor 22. At low speed the controller provides current in a trapezoidal form and at higher speeds, the current is sinusoidal. Also the drive system suffered from too low power ratings (which made it hard to go uphill) and significant torque ripples. This controller and its predecessor *WaveSculptor 20* are disassembled. The components that are visible are evaluated and the reconstructed schematic is shown in Figure 4.8.

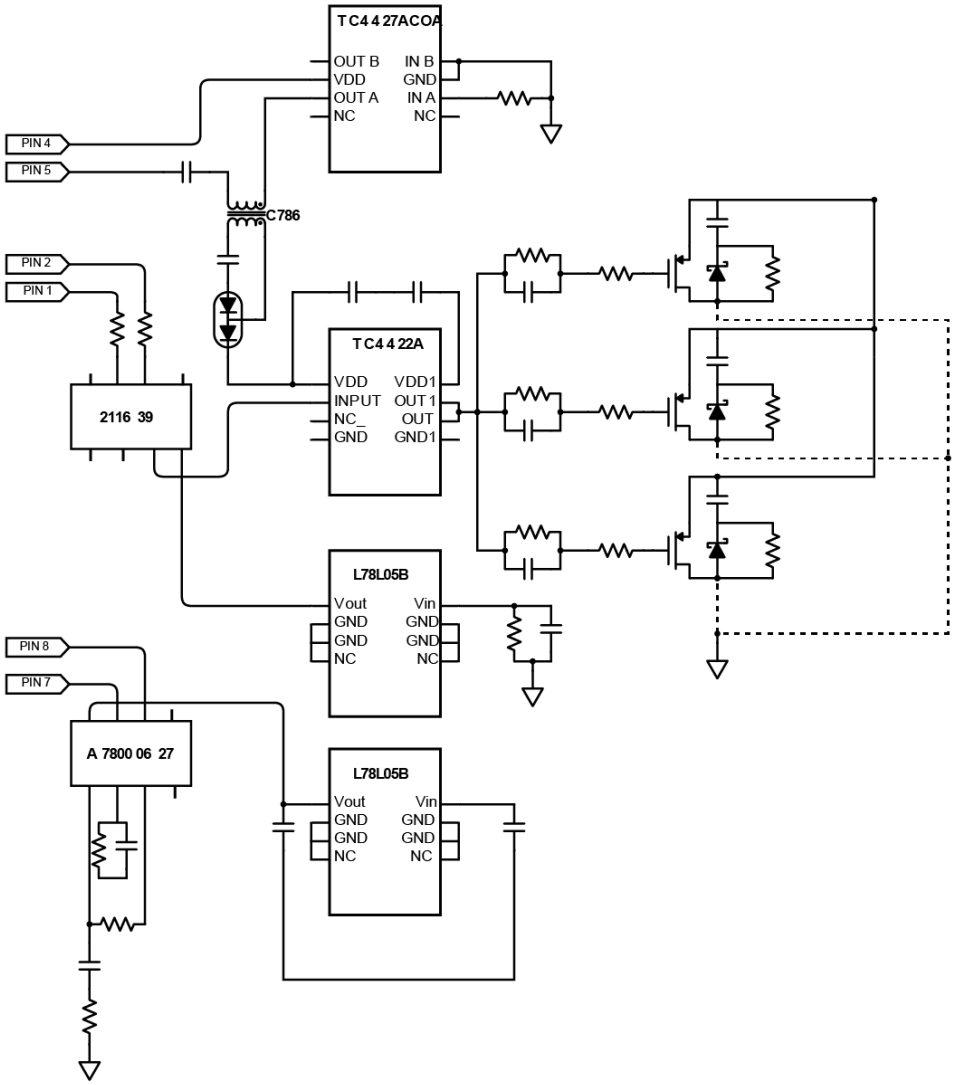

Figure 4.8: Highside gate drive of the Tritium 20 motor controller

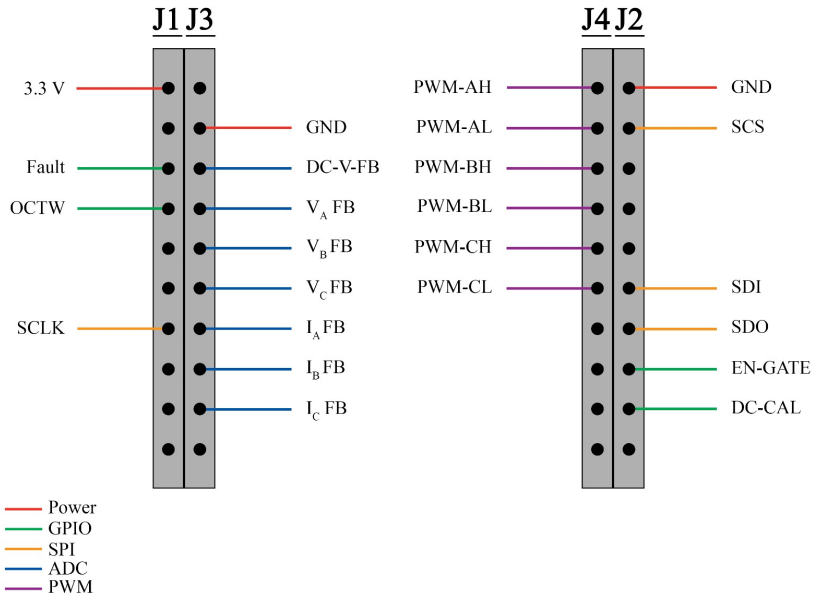

Figure 4.9: Pin lay-out of launchXL, different colors represent different signal types[30]

The inverter is built with 3 MOSFETs per phase per side parallel. These MOSFETs are driven by the gate driver TC4422A, a 9A high-speed MOSFET driver. On the high-side, the current is amplified by what seems either two optocouplers or two darlington transistors (211 639/211 044 and A 7800 0627). This is needed, because the current that needs to be controlled by the MOSFETs is much higher than the current the MOSFETs are driven by. Also a second voltage source is integrated to supply the chips and to decouple and protect the low-current part of the inverter. This is done by a C786 pulse transformer.

The Mitsuba motor comes with its own motor controller. This controller provides a power high enough for the car, but is less efficient. This controller M1596C weights 3.0 kg and has a nominal voltage of 96V and an input voltage between 70 and 150V. It operates with a 120 degree square wave. This controller was not availa at the moment.

4.3. SPECIFICATIONS NEW MOTORCONTROLLER

Switching frequency MOSFETs Since the motor will be controlled by a sinusoidal current, the minimal switching frequency needs to be high. When using the TI launchpad the frequency should be at least 20 kHz. This also avoids noise disturbance. The higher the switching frequency, the better the sine wave approximation but this also incurs higher switching losses, which makes the controller less efficiency.

Input voltage The motor controller is connected to a 80-200V battery.

Input current The battery can deliver a maximum current of 60A.

Output current The output is sinusoidal. To be able to use the current Mitsuba motor in South-Africa, the output current needs to go up to 150A. The instantaneous current of the motor may not exceed 200Arms. Moreover, the$_{po}$wer usage needs to be bi-directional, to allow regenerative braking.

Temperature sensors The temperature of the MOSFETs needs to be measured accurately and sent via CAN to monitor it.

Connection with LaunchXL This inverter can be connected to the LaunchXL-F28069M[29]. The pin lay out of the current inverter is shown in figure 4.9. In the thesis *Implementation of sensorless field oriented motor control in a solar car*[30] the set up of this controller can be found.

The following pins are going out of the inverter and to the controller:

- 3.3V; this signal is needed for the LaunchXL, and is provided from the TI-inverter board, but it would be better to separate the power of the LaunchXL from the inverter.
- Fault detection; this is a signal from the inverter after a shutdown event
- Over current and over temperature warning
- SPI signals; the LaunchXL is designed to communicate with different modules of TI-inverter boards. The SPI signals are used to set registers on the currently used TI-inverter board. This signals might be overwritten with other information when the inverter parameters are known and can be hardcoded in the controller. (These signals are actually bi-directional, but are only used one-directional.)
- ADC-signals; these signals are the measured currents and voltages between the inverter and motor. This should also be part of the inverter circuit. This is explained in more detail in the thesis *Implementation of sensorless field oriented motor control in a solar car*[30].
- Enable gate; This enables the gate drivers.
- DC calibration,...
- Other signals can be programmed on the remaining pins of the controller, like the temperature.

The following signals will go into the inverter module and come from the LaunchXL:

- 6 PWM signals; 2 per phase; high-side and low-side.

5

DRIVE SIMULATION

The drive model is constructed with the goal to test the compatibility of motor and drive. It is important to test both the efficiency of the motor and drive, as well as the combination of the two to see where precious energy can be saved. Furthermore, in such a simulation also the torque can be calculated, which makes it possible to check if the car will also meet the requirements of the demanded torque.

The model is built within the Simulink environment. The choice for Simulink was made for the following reasons:

- Familiarity with the program
- Integration with Matlab
- Extensive libraries of components and examples available

As the other group within the team was working on a Field Oriented Control, it was decided that the motors should be tested with this control method as well and that the rest of the components should match the real setup as closely as possible. The entire model can be seen in Figure C.1.

The model is compromised of the following parts which will be investigate further:

- A Field Oriented Control Algorithm Block
- A three phase inverter with battery connection
- A Permanent Magnet Synchronous Motor
- Some measurement instruments

The PMSM Field Oriented Control block is a block from the Simscape Power Systems package [31], which is not standard installed with Simulink. One can choose to implement either velocity or torque control with the Control mode parameter.

It takes a reference speed or torque, the 3 phase currents, DC-link voltage, the measured angle and mechanical angular velocity of the rotor.

It outputs six pulse waveforms that determine switching behaviour in the attached power converter. All inputs and outputs and some other intermediary signals are possible to visualize using the Visualization port. In the settings, all parameters of the PI controllers, gain and control methods can be adjusted.

The inverter block models as three-leg, two level inverter model. A detailed view can be seen in Figure 5.2. The inverter is like the Tritium controller constructed from 6 MOSFET transistors. Care should be taken with selecting a MOSFET with a low enough threshold voltage. The three phases are fed into a splitter to combine the signals on one line.

The Permanent Magnet Synchronous Motor block takes the most important motor variables, the motor constant, d- and q-inductances and stator resistance. The connected resistor provides a very small conductance to ground that improves numerical properties of the model when using a variable-step solver.

The motor is connected to an encoder, which employs a ideal torque and motion sensor and is connected to a source of inertia which models the motor & load.

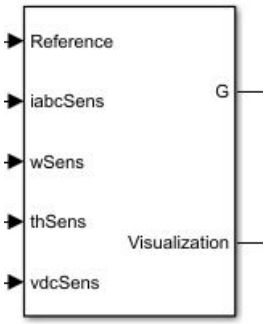

Figure 5.1: PMSM Field Oriented Control Block

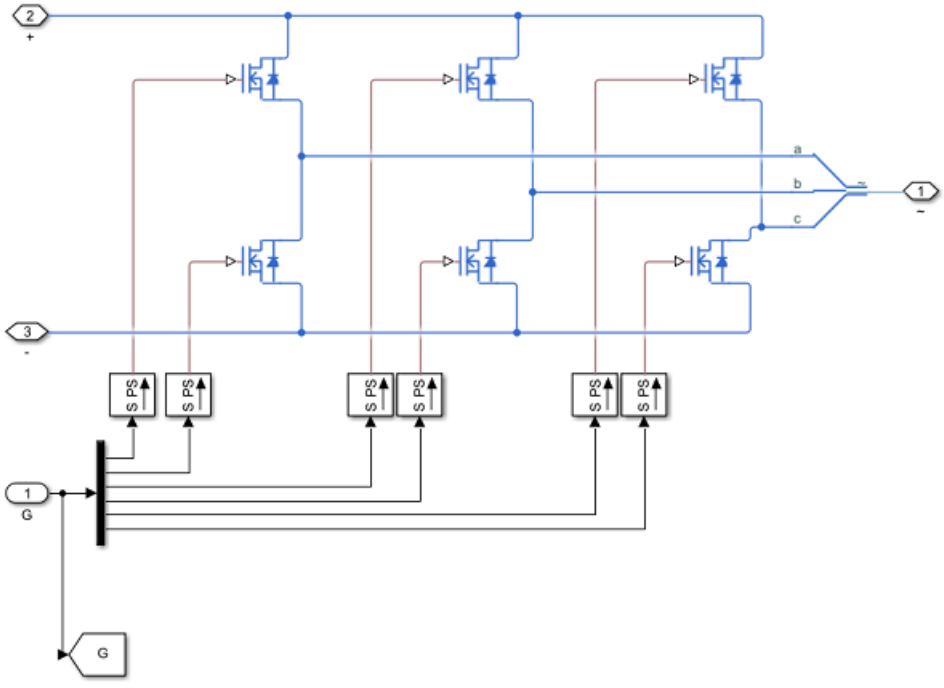

Figure 5.2: Inverter used in the Simulink simulation

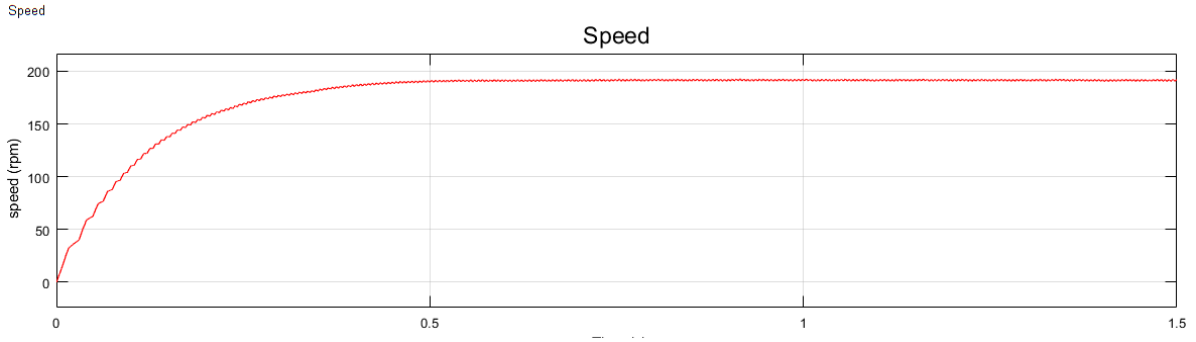

Figure 5.3: Speed curve simulated with Simulink model

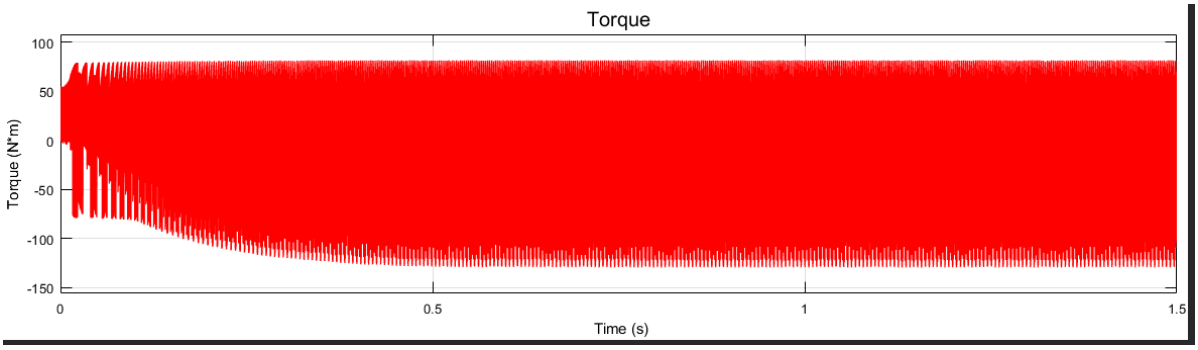

Figure 5.4: Torque curve simulated with Simulink model

Speed and torque curves have been plotted. In the case of Figure 5.3 and 5.4, this has been done using the components described above and the parameters from the Marand datasheets [17] and measurements. The speed plot is a smooth curve with the desired gentle ramp, but the torque does not produce a stable output yet. A torque of up till 75 Nm can be produced, but the system is too sensitive to the high speed measurement changes. This should become avoidable when fine tuning the parameters of the PI controllers.

6

Conclusion and Recommendations

6.1. Conclusion

Putting everything together, it can be seen that the group was successful in developing a model for the dominant motor types, being a radial and an axial flux machine. Key characteristics, which used to be hidden, are brought to the surface, like flux distributions and back EMF shape.

From literature study and theoretical research, it was decided that a finite element analysis would be appropriate. This would fill the hole left by the motor, which was still in transit from Australia during the entire project duration. The motor model would be used to gain access to insights about fundamental motor properties, with the most important question: what does the back EMF look like? What is the resistance, inductance and motor constant?

During the process the model was developed and improved. Also different calculations and simulations were developed so that a static program could also display dynamic behaviour.

The models in this report can be used to verify variations to the current motor designs. Things that a relatively easy to change like the windings or the magnets used / arrangement can be evaluated with this model.

The accuracy however is still somewhat limited. Boundary effects are not taken into account because it is a 2D model, eddy current and hysteresis not yet play a role in the calculations and not all material properties were known. It should therefore not be used for absolute measurements but for relative comparisons and quick simulations.

6.2. Future Work

Some work can be done to further improve the results in this report:

- Knowing the exact material of the rotor back iron.
- More accurate properties of magnets used.
- Find out more specifications of the motors
- Improve stability of Simulink model by adjusting the PI control parameters.
- Find or develop a suitable inverter to be used in combination with the TI FOC board developed by the other group.

Accurate material properties will improve the accuracy of the model. Also adding a loss model for eddy currents and hysteresis improves the quality of the simulation.

Another major hurdle that needs to be taken in order to get a fully operational motor control unit, is the inverter. Within this project, it was not possible to work on the inverter itself as so little was known about the motor and the Tritium controller. Now that some pieces of the puzzle are in place, a design can be made along some of the requirements that are drawn up by the Nuon Solar Team and that follow from the work done by the group.

The drive control hardware can be tested through the Simulink model. However the parameters for the PI controller need to be adjusted to make the Simulink simulation less sensitive to changes. With better knowledge of the motors this model will give more reliable results. Using the inverter model, requirements for a new inverter can be drawn up. A full research to a new inverter will be done by a MSc student under supervision of dr. ir Jianning Dong.

A

MITSUBA

A.1. INSTRUCTIONS

Guide to run the built simulations on your own PC.

1. Install FEMM on PC from the FEMM website.[14]
2. Add FEMM mfiles to Matlab via the interactive pathtool command from the Matlab Command Window.
3. Add the to be evaluated model .fem file and the matlab script to the Matlab folder or add the destination folder to path.
4. Run script. FEMM will automatically open the model, perform analysis and output results. (In order to reduce simulationt time, several calculations can be turned of for the duration of one simulation run.)

New FEMM models can be build by hand, through Matlab commands, Lua scripting or by importing 2D DFX files. The Magnetics tutorial on the FEMM website is highly recommended as well as the short attached manual before starting building models to get familiar with the environment. The tutorial takes about 15 - 25 minutes, getting familiar with building geometries less than a few hours.

A.2. SCRIPT

```
% Bachelor Graduation Project 2017
% Declan Buist & Elke Salzmann
% For the Nuon Solar Team
% 06-12-2017

%% Parameter definition
% This part initializes the parameters needed for the following scripts.

% The following parameters depend on the motor you want to model:
    MyModel = 'Mitsuba_motor.fem';
    BaseSpeed = 1128;        % base speed of the motor in RPM
    wbase=BaseSpeed/60;      % base frequency in Hz
    Axial_length = 0.040;    % In case of a radial-flux motor, this is the
                             % length of the motor

    % range of speeds
    SpeedMin = 0/60;         % in Hz
    SpeedMax = 1400/60;      % in Hz
    SpeedStep = 100/60;      % in Hz

    % Magnet properties
    RotorMagnets = 32;
    omag = 0.667*10^6;  % conductivity of NdFeB in S/m

% The following parameters are independent of the motor you are using,
% but can be changed according to the wishes of the simulations.
```

```
27
28      % Winding properties
29      MyIdCurrent = 20; % direct current in phase current amplitude scaling
30      MyIqCurrent = 20; % quadrature current phase current amplitude scaling
31
32      % angle increment in degrees
33      dk = 1;
34
35      %% Rotation
36  % This part simulates the rotation of the motor. It exports an image of the
37  % field lines.
38  dAlfa=9; % This is the angle with which the rotor will be rotated.
39
40  % When you installed femm according to the installation guide, you can run
41  % the simulation completely from Matlab with the following commands. It
42  % opens FEMM, opens your model and saves it in a seperate file to make sure
43  % that the simulation doesn't change the model.
44  openfemm
45  opendocument(MyModel)
46  mi_saveas('temp.fem')
47
48  % Problem definition, for more options, consult the FEMM manual.
49  freq=0; %Hz
50  mi_probdef(freq,'meters','planar',1e-8,Axial_length,30)
51
52  % The for-loop makes the rotor rotate and saves an image of the field
53  % density.
54  for n=1:dk:(180/dAlfa+1)
55    %First it analyses the model and shows the solution in FEMM.
56      mi_analyse(1)
57    mi_loadsolution()
58
59    mo_showdensityplot(0,0,0.16,0,'mag')     % Obtain Image of the model
60    alfa=dAlfa*(n-1);
61      filename=sprintf('acgen_%d.png', alfa);
62    mo_savebitmap(filename)                  % Save Image
63    mo_close()
64
65      % To rotate the rotor, group 1 is selected. In the FEMM-model all parts
66      % (all lines and material points) part of the rotor should be assigned
67      % to group 1 before running the simulation. Then, the selected group is
68      % rotated are point (0,0) with dAlfa degrees.
69    mi_selectgroup(1)
70    mi_moverotate(0,0,dAlfa)
71  end
72
73  %% Lock phase
74  % This section calculates the maximum flux linkage of phase A, this is
75  % needed to find the beginning position of the rotor. After this
76  % calculation the rotor in the simulation model should be turned to the
77  % angle for which the flux linkage is maximum. The rotor is in that case
78  % aligned with phase A.
79  openfemm;
80  opendocument(MyModel);
81  mi_saveas('temp.fem')
82
83  % The phase currents can be set here.
84  mi_setcurrent('A', 20);
85  mi_setcurrent('B', 0);
86  mi_setcurrent('C', 0);
87
88  fluxLinkageA=zeros(1,24);
89  for k = 0:1:23
90      mi_analyse(1)
91      mi_loadsolution()
92
93      % The properties of the circuits of an analyzed model can be obtained
94      % from FEMM. mo_getcircuitproperties() returns a vector with the
95      % current, voltage drop and flux linkage of the circuit.
96      propA = mo_getcircuitproperties('A');
97      fluxLinkageA(k+1)=real(propA(3));
```

```
98      mo_close()
99
100     mi_selectgroup(1)      % Select Rotor
101   mi_moverotate(0,0,dk)        % Rotate the rotor
102 end
103
104 %% Inductance
105 % This section calculates the phase inductance using the flux linkage.
106 % We assume that the inductance of every phase is the same,
107 % so we calculate it for one phase.
108 % This is only possible if the rotor is 'locked' to phase A.
109 openfemm;
110 opendocument(MyModel);
111 mi_saveas('temp.fem')
112
113 % This current is an arbitrary number, it can be anything.
114 I_a=20;
115
116 % First, the current of phase A is set to the positive voltage and B and C
117 % are connected to ground. So in the simulation this means that the current
118 % flows from A through B and C. The flux linkage of circuit is obtained.
119 mi_setcurrent('A', I_a);
120 mi_setcurrent('B', -I_a/2);
121 mi_setcurrent('C', -I_a/2);
122
123 mi_analyze(1)
124 mi_loadsolution()
125
126 propL = mo_getcircuitproperties('A');
127 fluxLinkageL=propL(3);
128 mo_close;
129
130 % Second, the current is turned around and the flux linkage is obtained.
131 mi_setcurrent('A', -I_a);
132 mi_setcurrent('B', I_a/2);
133 mi_setcurrent('C', I_a/2);
134
135 mi_analyze(1)
136 mi_loadsolution()
137
138 propM = mo_getcircuitproperties('A');
139 fluxLinkageM=propM(3);
140 mo_close;
141
142 % The inductance can be calculated with the following equations, the
143 % derivation can be found in the thesis.
144 L_a=(fluxLinkageL-fluxLinkageM)/I_a;
145 L_d=2/3*L_a;
146
147 %% Back-EMF
148 % This section calculates the back-EMF constant of the motor.
149 openfemm;
150 opendocument(MyModel);
151 mi_saveas('temp.fem')
152
153 freq=0; %Hz
154 mi_probdef(freq,'meters','planar',1e-8,0.040,30)
155
156 fluxLinkageB=zeros(1,48);
157 for k = 0:dk:47
158     % The current is set according to the transformations explained in the
159     % thesis.
160     theta=(RotorMagnets/2)*k*pi/180; % This is only possible if the magnets
161                                      % are not a halbach array
162     Id = [cos(theta), cos(theta-2*pi/3), cos(theta+2*pi/3)];
163     Iq =-[sin(theta), sin(theta-2*pi/3), sin(theta+2*pi/3)];
164     Itot =  MyIdCurrent*Id + MyIqCurrent*Iq;
165     mi_setcurrent('A', Itot(1));
166     mi_setcurrent('B', Itot(2));
167     mi_setcurrent('C', Itot(3));
168
```

```
169     mi_analyse(1)
170     mi_loadsolution()
171
172     prop = mo_getcircuitproperties('B');
173     fluxLinkageB(k+1)=real(prop(3));
174     mo_close()
175
176     mi_selectgroup(1)      % Select Rotor
177   mi_moverotate(0,0,dk) % Rotate the rotor
178 end
179
180 backEMF=zeros(1,47);
181 for n=1:dk:47
182     backEMF(n)=(fluxLinkageB(n+1)-fluxLinkageB(n));
183 end
184 plot(backEMF)
185
186 %% Torque
187
188 % open up the base geometry file
189 openfemm;
190 opendocument(MyModel);
191 mi_saveas('temp.fem')
192 mi_probdef(0,'meters','planar',1e-8,Axial_length,30);
193
194 torque=zeros(1,24);
195 for k=0:1:23
196     mi_analyze(1)
197   mi_loadsolution()
198     mo_groupselectblock(1);
199     torque(k+1)=mo_blockintegral(22);
200     mo_close;
201
202    % rotate the rotor to the position for the next iteration.
203     mi_selectgroup(1);
204     mi_moverotate(0, 0, 1);
205
206     fprintf('%i of 24 ::  %f N*m \n',k+1,torque(k+1));
207 end
208 plot(0:1k:23,torque)
```

B

MARAND

```
%% Start User-Defined Parameters
%%%%%%%%%%%%%%%%%%%%%%%%%%%%%%%%%%%%%%%%

% Model Name
MyModel = 'versie2halbach.fem';

% base frequency in Hz
wbase=4000/60; %(4000 rev/minute)*(minute/(60*seconds))

% range of speeds over which to evaluate losses
SpeedMin = 100; % in RPM
SpeedMax = 8000; % in RPM
SpeedStep = 100; % in RPM

% Winding properties
MyIdCurrent = 0; % direct current in phase current amplitude scaling
MyIqCurrent = 2; % quadrature current phase current amplitude scaling
AWG=25; % Magnet wire gauge used in winding
PhaseResistance = 0.0575; % phase resistance

% Magnet properties
RotorMagnets = 40; %(2x 40 magnets=80)
pp = RotorMagnets/2;   %#pole pairs
omag = 0.556*10^6;          % conductivity of sintered NdFeB in S/m



%%%%%%%%%%%%%%%%%%%%%%%%%%%%%%%%%%%%%%%%
%% End User-Defined Parameters
%%%%%%%%%%%%%%%%%%%%%%%%%%%%%%%%%%%%%%%%

% helpful unit definitions
PI=pi; Pi=pi;
deg=Pi/180.;

% distance over which to move coils
d = 4;

% step size
dk = 0.25;

%% Perform a series of finite element analyses

openfemm;   %opens Finite Elements Method Magnetics
opendocument(MyModel);    %Opens model stored in variable MyModel
smartmesh(1);  %auto mesh setting
mi_saveas('temp.fem');    %create a temp file, so original model is not changed by looping

for k=0:dk:d       % start loop for a distance d with step size dk
    kk = k/dk + 1;    %necessary variable for vector length
```

```
    % Record flux density
    mi_analyze(1);        %initializes magnetics solver, 1 makes solver window visible
    mi_loadsolution;      %loads and displays the solution corresponding the current geometry
    if (k==0)
        %Record the initial mesh elements if the first time through the loop
        nn = mo_numelements;   %stores number of mesh elements
        % create empty arrays for storing data
        b = zeros(floor(d/dk),nn);       %flux density
        A = zeros(floor(d/dk),nn);       %vector potential
        E = zeros(floor(d/dk),nn);       %EMF
        x = zeros(nn,1);                 %x-coordinate mesh element
        y = zeros(nn,1);                 %y-coordinate mesh element
        a = zeros(nn,1);                 %area mesh element
        g = zeros(nn,1);                 %group number mesh element
        torque = zeros(d/dk,1);          %torque
        linkageA = zeros(floor(d/dk),1);%flux linkage phase A
        linkageB = zeros(floor(d/dk),1);%flux linkage phase B
        linkageC = zeros(floor(d/dk),1);%flux linkage phase C
        for m = 1:nn
            %mo_getelement returns a list of properties for the mth element
            %store list in vector elm
            elm = mo_getelement(m);
            %get x-coor of mesh element m
            x(m)=elm(4);
            %get y-coor of mesh element m
            y(m)=elm(5);
            %get area of mesh element m
            a(m)=elm(6);
            %get group number of mesh element m
            g(m)=elm(7);
        end
    end

% g = 0 > AIR // g = 1 > COILS // g = 11 > UPPER ROTOR // g = 12 > BOTTOM
% ROTOR

    for m = 1:nn
       if(g(m)==1) % Element is on the coils
           % mo_getpointvalues returns a list of values associated with
           % point at (x,y)
           %store list in vector pv
           pv = mo_getpointvalues(x(m),y(m));
           b(kk,m) = pv(2)+pv(3);   %places value of Bx and By in array b
           A(kk,m) = pv(1);         %places value of potential A in array
       end
       if(g(m)>10) % Element is on the rotors
           pv = mo_getpointvalues(x(m),y(m));
           b(kk,m) = pv(2)+pv(3);
       end
    end


    % loop the coils through the motor
    for k=0:dk:d
        mo_groupselectblock(1) %Select block(s) on which operations will be carried out
    end
    %torque(kk)= mo_blockintegral(22);    %Performs a Maxwell stress tensor
    %calculation on selected block to find torque
    % A(kk) = mo_blockintegral(2);       %Calculates vector potential
    circuitA = mo_getcircuitproperties('A');    %get circuit properties of phase A, returns a list stored
     in vector circuitA
    circuitB = mo_getcircuitproperties('B');    %"" for B
    circuitC = mo_getcircuitproperties('C');    %"" for C

    linkageA(kk) = circuitA(3);          %stores flux linkage in variable linkageA
    linkageB(kk) = circuitB(3);          %"" for B
    linkageC(kk) = circuitC(3);          %"" for C

    E = diff(linkageA)*pp*wbase;         %Calculates Back EMF from flux linkage, pole pairs and base speed

    for k=0:dk:15           %select group 1(==coils)
```

```
121             mi_selectgroup(1)
122         end
123         mi_movetranslate(dk,0) %translate the coils a distance dk
124 
125         %% Flux Linkage Plot
126         plot(0:dk:d-0.5,E,'-s');
127         title('Back EMF')
128         xlabel('Rotor Angle, Degrees')
129         ylabel('Voltage, Volt')
130         grid on
131 
132 %       %% Torque plot
133 %         plot(0:dk:d-0.5,torque);
134 %         xlabel('Rotor Angle, Degrees');
135 %         ylabel('Torque, N*m');
136 %         title('Torque on Rotor vs. Angle');
137 
138 % %% Vector Potential Plot
139 %         plot(0:dk:d-0.5,A);
140 %         xlabel("Coil position, cm");
141 %         ylabel("A");
142 %         title("Magnetic Vector Potential vs Position");
143 
144         %add contour in the middle of the airgap for measurements purposes
145         %mo_addcontour(1,0.45)
146         %mo_addcontour(21.5,0.45)
147 end
```

C

SIMULINK

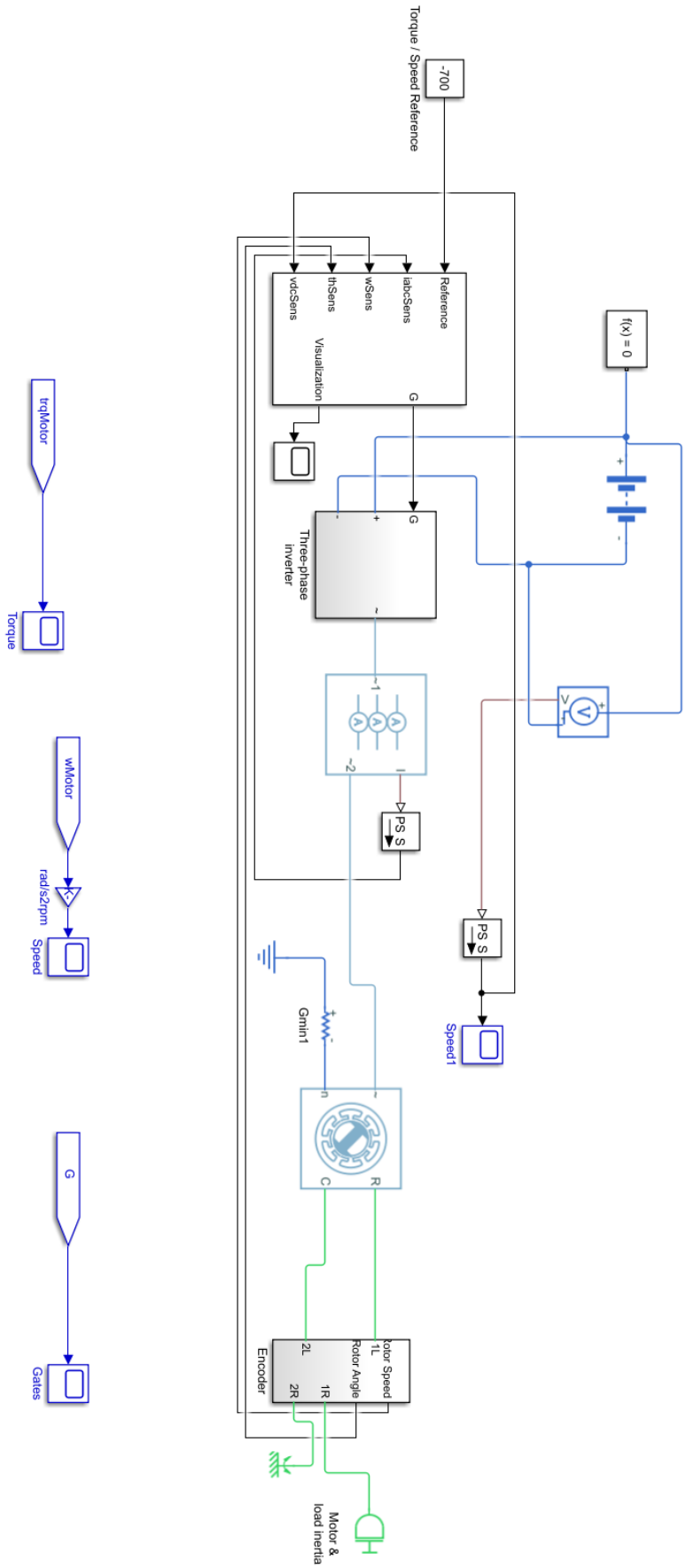

Figure C.1: Simulink model of the motor, inverter and FOC

D

DATASHEETS

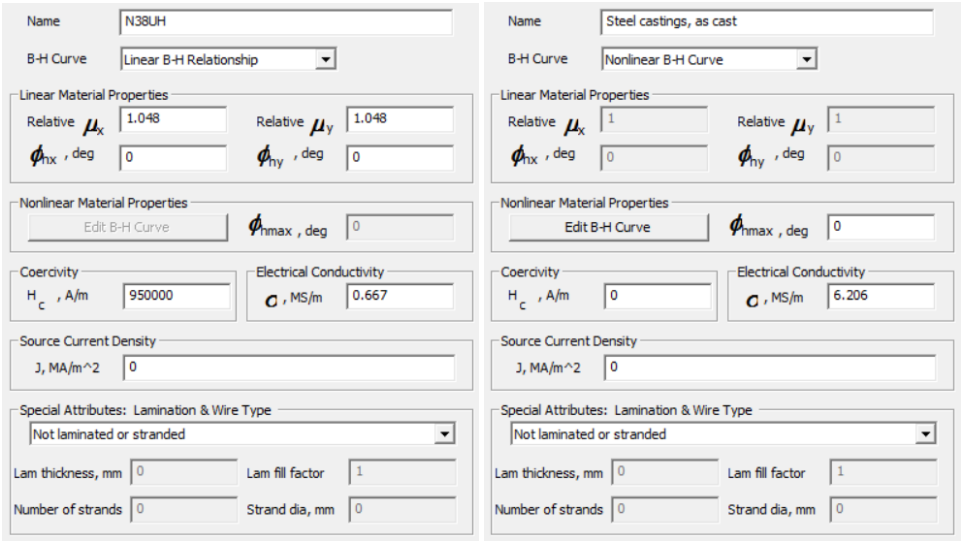

(a) Material rotor magnets

(b) Material stator steel

(c) Material windings

(d) Material back-iron

Figure D.1: Properties of the materials used for the simulation of the Mitsuba motor

BIBLIOGRAPHY

[1] K. H. Nam, *AC Motor Control and Electric Vehicle Applications* (CRC Press, 2010).

[2] J. Mevey, *Sensorless field oriented control of brushless permament magnet synchronous motors,* (2009).

[3] R. Krishnan, *Permanent Magnet Synchronous and Brushless DC Motor Drives* (CRC Press, 2010).

[4] E. P. A. T. L. Ferraris, P. Ferraris, *Comparison between parallel and radial magnetization in pm fractional machines,* in *IECON 2011 - 37th Annual Conference on IEEE Industrial Electronics Society* (IEEE, 2011).

[5] G. C. Lidija Petkovska, *Comparative analysis of magnetic field in surface permanent magnet motor at various types of rotor magnetization,* .

[6] M. Yilmaz, *Limitations/capabilities of electric machine technologies and modeling approaches for electric motor design and analysis in plug-in electric vehicle applications,* (Elsevier, 2015).

[7] F. Meier, *Permanent-magnet synchronous machines with non-overlapping concentrated windings for low-speed direct-drive applications.* (2008).

[8] Emetor, *Online electric motor design software,* https://www.emetor.com/edit/windings/.

[9] D. H. Z. Q. Zhu, *Electrical machines and drives for electric, hybrid, and fuel cell vehicles,* in *Proceedings of the IEEE* (IEEE, 2007).

[10] S. Derammelaere, M. Hamers, J. de Viaene, F. Verbelen, and K. Stockman, *A quantitative comparison between bldc, pmsm, brushed dc and stepping motor technologies,* in *2016 19th Internation Conference on Electrical Machines and Systems (ICEMS)* (IEEE, 2016).

[11] F. M. . P. T. . C. Sadarangani, *Performance evaluation of permanent magnet synchronous machines with concentrated and distributed windings including the effect of field-weakening,* in *Second International Conference on Power Electronics, Machines and Drives* (IEEE, 2004).

[12] *Sensorless PMSM Field-Oriented Control*, NXP Semiconductors.

[13] W. Yao, H. Hu, and Z. Lu, *Comparisons of space-vector modulation and carrier-based modulation of multilevel inverter,* IEEE Transactions on Power Electronics **23**, 45 (2008).

[14] *Finite elements method magnetics (femm),* http://www.femm.info.

[15] *Nuna Motor Review*, AE Group Advanced Electromagnetics.

[16] J. S. F. Libert, *Investigation on pole-slot combinations for permanent-magnet machines with concentrated windings,* .

[17] *Marand Electric Machines*, Marand.

[18] A. Egea, G. Almandoz, J. Poza, and A. Gonzalez, *Axial flux machines modelling with the combination of 2d FEM and analytic tools,* in *The XIX International Conference on Electrical Machines - ICEM 2010* (IEEE, 2010).

[19] S. W. Colton, *Design and prototyping methods for brushless motors and motor control,* (2010).

[20] D. Martinez, *Design of a permanent-magnet synchronous machine with non-overlapping concentrated windings,* (2012).

[21] H. Lovatt, *Design of an in-wheel motor for a solar-powered electric vehicle,* in *Eighth International Conference on Electrical Machines and Drives* (IEEE, 1997).

[22] V. Bobek, *PMSM Electrical Parameters Measurement*, NXP Semiconductors.

[23] H. Y. H. K. Jih-sheng Lai, Junhong Zhang, *Source and load adaptive design for a high-power soft-switching inverter,* in *IEEE Transactions on Power Electronics* (IEEE, 2006).

[24] A. E. Haizhong Ye, Yinye Yang, *Traction inverters in hybrid electric vehicles,* Transportation Electrification Conference and Expo (2012).

[25] T. G. H. Leon M. Tolbert, Fang Z. Peng, *Multilevel inverters for electric vehicle applications,* Power Electronics in Transportation, 1998 (1998).

[26] S. Kharjule, *Voltage source inverter,* (2015).

[27] C. B. Carl Blake, *Igbts or mosfets: Which is better for your design?* (1999).

[28] W. Zhang, Y. Long, Z. Zhang, F. Wang, L. M. Tolbert, B. J. Blalock, S. Henning, C. Wilson, and R. Dean, *Evaluation and comparison of silicon and gallium nitride power transistors in llc resonant converter,* Energy Conversion Congress and Exposition (2012), 10.1109/ECCE.2012.6342657.

[29] *Launchxl-f28069m overview,* in *User's guide* (Texas Instruments, 2015).

[30] T. R. J. Bout, *Implementation of sensorless field oriented motor control in a solar car,* (2018).

[31] Simscape, *Online electric motor design software,* https://nl.mathworks.com/products/simpower.html.